Geoscience Frontiers xxx (xxxx) xxx

HOSTED BY

ELSEVIER

Contents lists available at ScienceDirect

Geoscience Frontiers

journal homepage: www.elsevier.com/locate/gsf

Research Paper

Resistivity of reservoir sandstones and organic rich shales on the Barents Shelf: Implications for interpreting CSEM data

Kim Senger [a,*], Thomas Birchall [a,b], Peter Betlem [a,b], Kei Ogata [c,d], Sverre Ohm [a,e], Snorre Olaussen [a], Renate S. Paulsen [a,f]

[a] Department of Arctic Geology, The University Centre in Svalbard, Longyearbyen, Norway
[b] Department of Geosciences, University of Oslo, Oslo, Norway
[c] Department of Earth Science, Vrije Universiteit, Amsterdam, Netherlands
[d] Now at Dipartimento di Scienze Della Terra, Dell'Ambiente e Delle Risorse (DISTAR), Università Degli Studi di, Napoli Federico II, Napoli, Italy
[e] Department of Energy Resources, University of Stavanger, Stavanger, Norway
[f] Department of Geosciences, University of Tromsø – the Arctic University of Norway, Tromsø, Norway

ARTICLE INFO

Keywords:
Barents Shelf
Petroleum
Electromagnetic
Exploration
Source rocks

ABSTRACT

Marine controlled source electromagnetic (CSEM) data have been utilized in the past decade during petroleum exploration of the Barents Shelf, particularly for de-risking the highly porous sandstone reservoirs of the Upper Triassic to Middle Jurassic Realgrunnen Subgroup. In this contribution we compare the resistivity response from CSEM data to resistivity from wireline logs in both water- and hydrocarbon-bearing wells. We show that there is a very good match between these types of data, particularly when reservoirs are shallow. CSEM data, however, only provide information on the subsurface resistivity. Careful, geology-driven interpretation of CSEM data is required to maximize the impact on exploration success. This is particularly important when quantifying the relative resistivity contribution of high-saturation hydrocarbon-bearing sandstone and that of the overlying cap rock. In the presented case the cap rock comprises predominantly organic rich Upper Jurassic–Early Cretaceous shales of the Hekkingen Formation (i.e. a regional source rock). The resistivity response of the reservoir and its cap rock become merged in CSEM data due to the transverse resistance equivalence principle. As a result of this, it is imperative to understand both the relative contributions from reservoir and cap rock, and the geological significance of any lateral resistivity variation in each of the units. In this contribution, we quantify the resistivity of organic rich mudstone, i.e. source rock, and reservoir sandstones, using 131 exploration boreholes from the Barents Shelf. The highest resistivity (>10,000 Ωm) is evident in the hydrocarbon-bearing Realgrunnen Subgroup which is reported from 48 boreholes, 43 of which are used for this study. Pay zone resistivity is primarily controlled by reservoir quality (i.e. porosity and shale fraction) and fluid phase (i.e. gas, oil and water saturation). In the investigated wells, the shale dominated Hekkingen Formation exhibits enhanced resistivity compared to the background (i.e. the underlying and overlying stratigraphy), though rarely exceeds 20 Ωm. Marine mudstones typically show good correlation between measured organic richness and resistivity/sonic velocity log signatures. We conclude that the resistivity contribution to the CSEM response from hydrocarbon-bearing sandstones outweighs that of the organic rich cap rocks.

1. Introduction

Seismic data, which rely on mapping the acoustic impedance (i.e. velocity × density) contrasts of the subsurface (Cartwright and Huuse, 2005), are routinely used to produce structural subsurface maps prior to drilling. The determination of subsurface fluids during petroleum exploration is, however, challenging when using seismic data alone. In particular, it is difficult to discriminate reservoirs with a high gas saturation from those with low saturation (i.e. the "fizz gas" effect; e.g., Han and Batzle, 2002). In contrast to sonic velocity, resistivity is only affected when hydrocarbon saturation exceeds 60%–70% (Constable, 2010; Hesthammer et al., 2010) and is the prime tool used to calculate

* Corresponding author.
E-mail address: kim.senger@unis.no (K. Senger).
Peer-review under responsibility of China University of Geosciences (Beijing).

https://doi.org/10.1016/j.gsf.2020.08.007
Received 4 November 2019; Received in revised form 25 June 2020; Accepted 4 August 2020

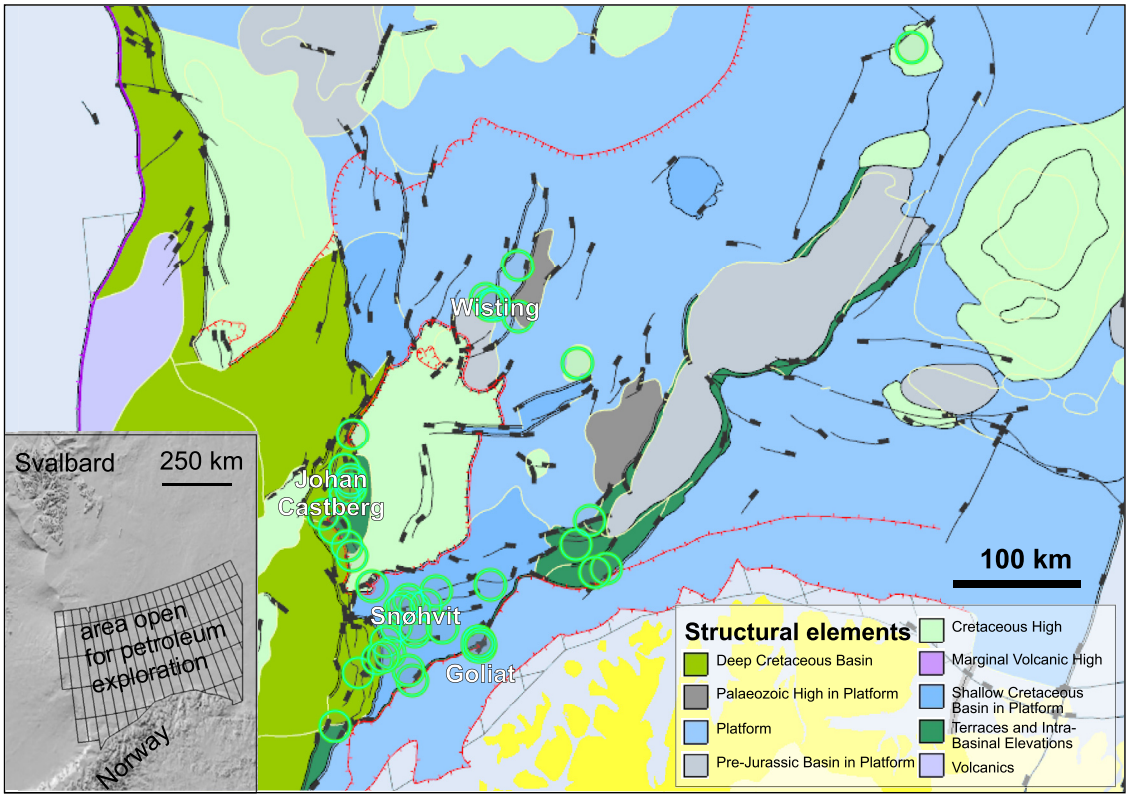

Fig. 1. Structural map of the study area, courtesy of NPD (2016). Wells with hydrocarbons within the Realgrunnen Subgroup are highlighted by green circles.

water saturation in pay zone intervals. Resistivity has been measured in virtually all exploration boreholes since Schlumberger started wireline logging in 1927 (Johnson, 1962). Much can be learned from resistivity wireline logs to improve and calibrate the interpretation of controlled source electromagnetic (CSEM) data. Furthermore, resistivity logs provide a direct comparison to pre-drill derived resistivity from CSEM data.

CSEM is primarily a marine data acquisition technique that has been used by the petroleum industry since the early 2000s (Eidesmo et al., 2002; Ellingsrud et al., 2002). As resistivity logs are complementary to other wireline logs, CSEM data are complementary to seismic data. Acquisition of CSEM data typically relies on towing a high-powered horizontal electric dipole source approximately 30 m above the seafloor to transmit a low-frequency electromagnetic signal through the seafloor (MacGregor and Tomlinson, 2014). Three-component nodal receivers placed on the seafloor record the electric and magnetic components (Constable, 2010; Johansen and Gabrielsen, 2015; MacGregor and Tomlinson, 2014). Inversion of CSEM data iteratively attempts to find an acceptable subsurface resistivity model that fits the actual measurements, thus providing subsurface resistivity cubes and profiles. Interpretation of CSEM resistivity data is non-trivial and relies on understanding two aspects, namely (1) how CSEM data are acquired and inverted, including careful consideration of the role played by CSEM sensitivity, and (2) what geological factors influence the subsurface resistivity distribution. Johansen and Gabrielsen (2015) provided a comprehensive overview of the acquisition, processing and inversion of CSEM and magnetotelluric (MT) data in hydrocarbon prospecting.

Typically, marine CSEM data are used to de-risk seismically-defined prospects by identifying and characterizing laterally constrained, high resistive anomalies thought to be associated with hydrocarbon saturation (Fanavoll et al., 2014; Johansen and Gabrielsen, 2015; MacGregor et al., 2012; Stefatos et al., 2014). A number of CSEM-driven leads developed on the basis of high resistivity anomalies have also been defined (Carstens, 2018; Stefatos et al., 2014). However, resistive anomalies can also be related to other geological factors, for instance tight sandstones, tight carbonates, mature source rocks, salt, fresh water, gas hydrates or igneous intrusions (e.g., Alvarez et al., 2018; Barker and Baltar, 2016; Evans, 2007; Schwalenberg et al., 2017; Senger et al., 2017b; Spacapan et al., 2019; Tharimela et al., 2019).

The main benefit of using CSEM is to quantify the subsurface resistivity distribution prior to drilling. As with any exploration technique, CSEM has its limitations and interpreters must be aware of potential pitfalls. One of the key aspects to consider with CSEM is its sensitivity to a given target. Sensitivity is governed by the target size (i.e. area), target transverse resistance (i.e. pay zone resistivity times pay zone thickness), target burial depth and structural and stratigraphic complexity of the background resistivity (MacGregor, 2012; MacGregor and Tomlinson, 2014). If properly integrated into the exploration workflow, CSEM data can be applied to de-risk prospects (Buland et al., 2011; Fanavoll et al., 2014; Gabrielsen et al., 2013), hydrocarbon saturation prediction prior to drilling (Løseth et al., 2014), optimizing a drilling strategy for a prospect portfolio (Zweidler et al., 2015), constraining gas hydrate systems (Tharimela et al., 2019; Weitemeyer et al., 2011), or delineating discoveries and constraining resource estimates (Baltar and Barker, 2015; Baltar and Roth, 2013). Many case studies where CSEM has been successfully used in exploration stem from the Barents Sea (e.g., Alvarez et al., 2018; Fanavoll et al., 2014; Gabrielsen et al., 2013; Granli et al.,

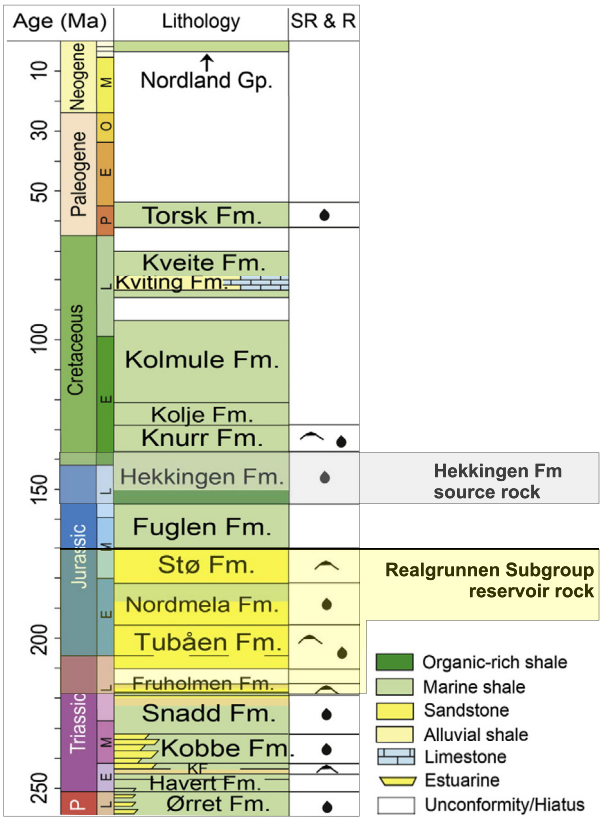

Fig. 2. Stratigraphic chart of the Barents Shelf, illustrating the major lithologies and tectonic events. Chart adapted from Duran et al. (2013), originally based on Ohm et al. (2008).

2017). Here, geological conditions are suitable for CSEM mapping, given the very high sensitivity of shallow reservoir targets (common to the Barents Shelf area), to CSEM.

Quantitative links between resistivity and its underlying geological drivers are still remarkably poorly documented. This is particularly the case for quantifying the contribution of organic rich shales directly overlying hydrocarbon-bearing sandstones to resistivity measurements. In this contribution, we summarize the published CSEM case studies from the Barents Sea and review exploration well results. Secondly, we quantify the resistivity variation in hydrocarbon-bearing sandstone reservoirs of the Upper Triassic to Middle Jurassic Realgrunnen Subgroup and the overlying source rock of the Upper Jurassic to Lower Cretaceous Hekkingen Formation with publicly available data from 43 boreholes (Fig. 1). Finally, we discuss the significance of the resistivity variation in the context of integrated interpretation of CSEM data together with seismic and borehole data.

2. The Barents Shelf: geological setting and exploration history

The geological history of the Barents Shelf is discussed at length in numerous publications (e.g., Faleide et al., 2008; Faleide et al., 1993; Grogan et al., 1999; Henriksen et al., 2011b; Worsley, 2008 and references therein) and is only briefly reviewed here. The western Barents Sea, i.e. the Norwegian sector and its onshore equivalent in Svalbard, can be considered as representing four major tectonic phases (Fig. 2; Henriksen et al., 2011b; Steel and Worsley, 1984; Worsley, 2008):

Phase one is defined by the Paleozoic Caledonian Orogeny and the subsequent Devonian denudation of the mountain chain in the western Barents Shelf (Steel and Worsley, 1984; Worsley, 2008);

The second phase involves Carboniferous to Permian extension with rift basins and rotated fault blocks with mixed siliciclastic, carbonate and evaporate basin fill (Worsley, 2008). Successful play concepts host the recent Gohta and Alta oil discoveries on the Loppa High (e.g., Matapour et al., 2019; Rønnevik, 2015);

The third phase is dominated by sag-basins and platform areas, apart from the western margin of the Barents Shelf. The tectonic and depositional setting in this area was initiated in the uppermost part of the Permian. Denudation of the Uralide mountain belt and northern Fennoscandian shield, coupled with continued subsidence in the Barents Sea, created a northwestward prograding shelf edge delta (e.g., Glørstad-Clark et al., 2010; Høy and Lundschien, 2011; Klausen et al., 2017; Klausen et al., 2019c). By the Early Norian, the system had prograded by approximately 1500 km to as far as central Spitsbergen in Svalbard (Anell et al., 2014; Klausen et al., 2019c). The lower pay zone in the Goliat oil field is partly producing from Middle Triassic sandstone reservoirs of the Kobbe Formation (Duran et al., 2013; Rossi et al., 2020). Reduced

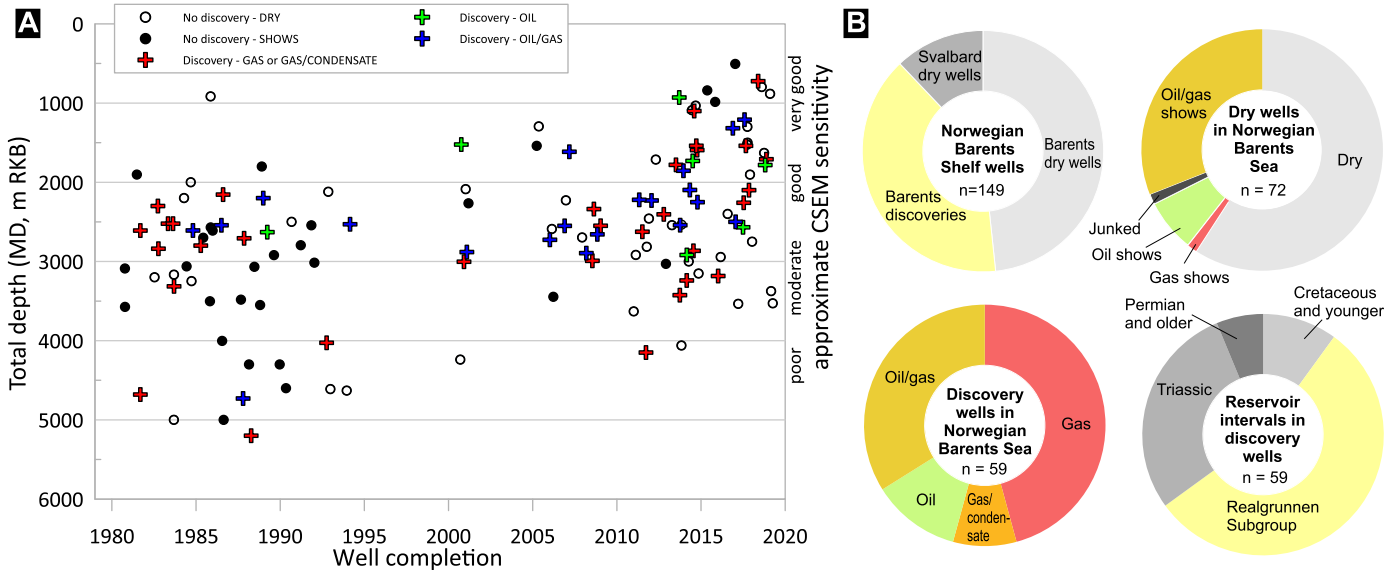

Fig. 3. (A) Overview of exploration activity in the Norwegian Barents Shelf as a function of time, borehole depth and borehole result. CSEM sensitivity is only indicated approximately, as it will be determined by the acquisition system used and the case-specific geological conditions. (B) Statistics on the success rate of boreholes and subdivision of boreholes by fluid type and main reservoir intervals. Data from NPD FactPages.

subsidence in the Upper Triassic (Ryseth, 2014), coupled with initiation of the Novaya Zemlya Fold and Thrust Belt, resulted in deposition of the condensed Upper Triassic to Lower Jurassic succession of the Realgrunnen Subgroup (Klausen et al., 2019a; Müller et al., 2019; Olaussen et al., 2018).

Along the western margin subsidence continued, allowing for thick Upper Triassic to Middle Jurassic deposits to accumulate. These are preserved as the thick sandstone-dominated formations of the Realgrunnen Subgroup. The Toarcian to Bajocian aged sandstone dominated succession of the Stø Formation, at the top of the Realgrunnen Subgroup, is so far the most prolific reservoir unit in the western Barents Sea (Lundschien et al., 2014). The unit is also well developed throughout large parts of the platform area. The Middle Jurassic to Lower Cretaceous organic rich mudstone-dominated succession, shows a gradually shift in source-to-sink trends, with drainage from the north and west with a dominantly southwards progradation of shorelines and shelf deposits (Grundvåg et al., 2017; Koevoets et al., 2019; Midtkandal et al., 2020). This shift in sediment dispersal throughout the northern Barents Shelf is likely associated with the opening of the Amerasian Basin to the north (Shephard et al., 2013). This can also be considered as occurring contemporaneously with significant magmatic activity associated with the emplacement of the High Arctic Large Igneous Province (HALIP; Senger et al., 2014).

On the western margin and along the southern boundary of the western Barents Sea, rifting and extension continued from the Late Permian onwards (Faleide et al., 1993, 1996; Serck et al., 2017). To date, the most successful play concepts in this area are related to this tectonic phase. The Snøhvit gas field, the upper pay zone in the Goliat oil field, the Johan Castberg oil field and the Wisting discovery all target Upper Triassic–Middle Jurassic sandstones in the Realgrunnen Subgroup (e.g., Klausen et al., 2019; Mulrooney et al., 2017; Wennberg et al., 2008). While the Upper Jurassic to lower Cretaceous Hekkingen Formation forms the source rock in the Snøhvit, Johan Castberg and Goliat (upper pay zone) fields, the Wisting discovery is sourced from the Middle Triassic Steinkobbe Formation (Lerch et al., 2018). The Hekkingen and Fuglen formations, together with lower Cretaceous shales, form the major cap rock of these accumulations (Abay et al., 2018; Henriksen et al., 2011b).

The fourth tectonic phase is characterized by major uplift and erosion. This initiated in the Late Cretaceous to early Paleogene by compression and shearing along the western margin of the Barents Sea, followed by rifting related to the final opening of the North Atlantic and crustal break-up and resulted in the current basin configuration (Faleide et al., 1993; Worsley, 2008). Consequently, the western margin is down-faulted and covered by thick successions of Late Cretaceous to Cenozoic sediments (Faleide et al., 1996; Serck et al., 2017). The Neogene culminated with glacial erosion during the Pliocene to Pleistocene throughout the Barents Sea area. In the western margin, Cenozoic net erosion varies from 100 s of meters to 3000 m (Henriksen et al., 2011a; Ktenas et al., 2017). Uplift and erosion is regarded as the single most important process for preservation of oil accumulations. Uplift may have led to the tilting of hydrocarbon traps, seal failure (e.g., fracturing or fault reactivation), and gas exsolution, all of which can lead to hydrocarbon remigration or phase change (Baig et al., 2016; Birchall et al., 2020; Cavanagh et al., 2006; Dimakis et al., 1998; Ohm et al., 2008). Furthermore, due to previous deep burial, the reservoir quality is reduced as a result of chemical and mechanical compaction (Henriksen et al., 2011a, 2011b; Mørk, 2013).

The Barents Sea is a frontier exploration province, estimated to contain 48% of undiscovered hydrocarbon resources on the Norwegian Continental Shelf, corresponding to approximately 1.4 billion Sm^3 (8809 MMboe) of oil equivalents (NPD, 2015). The area currently open to petroleum exploration in the Norwegian segment of the Barents Sea covers almost 300,000 km^2 (Fig. 1), where 131 exploration wells (i.e. one well per 2290 km^2) have been drilled offshore since the first exploration well, 7119/12–1, in 1980. In addition, 18 petroleum exploration boreholes were drilled onshore Svalbard, located at the north-western margin of the Barents Shelf, from 1961 to 1994 (Fig. 1; Nøttvedt et al., 1993; Senger et al., 2019).

Jakobsson (2018) provided a comprehensive overview of the licensing rounds, key discoveries and production starts since the first Barents Sea licensing round in 1980. Fig. 3A illustrates the drilling sequence along with a summary of the well results. There has been considerable drilling activity, especially since 2010, with many relatively shallow boreholes (<1.5 km beneath the seabed) with ultra-shallow discoveries like Wisting < 0.5 km beneath the seabed) targeting the Realgrunnen Subgroup in the northern part of the opened exploration acreage. Out of 131 exploration boreholes drilled as of today, 59 (i.e. 45%) are classified as discoveries (Fig. 3B). Approximately one third of the remaining 72 wells classified as "dry" still prove hydrocarbon shows (Fig. 3B). The NPD classification of a discovery wellbore requires that any quantity of moveable hydrocarbons is encountered. Most discoveries are gaseous, some with residual oil columns. Oil discoveries were made at Goliat, Johan Castberg and Wisting. The Realgrunnen Subgroup, targeted in this study, accounts for 55% of the hydrocarbon-bearing reservoirs (Fig. 3B). The residual oil columns indicate that many of the traps within the Realgrunnen Subgroup were previously filled to a structural spill point (Henriksen et al., 2011a; Ohm et al., 2008). Hydrocarbons likely migrated out of existing traps as a result of tilting, trap breaching or gas exsolution due to Cenozoic uplift (see above). Because of this, a key aspect to exploration success in the Barents Sea is the ability to predict the present-day fluid phase and overall hydrocarbon saturation in a prospect, prior to drilling. Here, CSEM data is highly complementary to seismic data, which struggle to differentiate between low-saturation "fizz-gas" and high-saturation "commercial gas" (Constable, 2010; Hesthammer et al., 2010). Resistivity, in contrast to seismic data, is only sensitive at hydrocarbon saturations exceeding ca. 60%–70%, and can thus be used to differentiate these (Carcione et al., 2007; Constable, 2010; Werthmüller et al., 2013). Importantly, both oil and gas are electrical insulators and resistivity data cannot distinguish between the phases.

3. Methods and data

For this study, we use data from both publicly available offshore exploration wells from the Barents Sea (DISKOS database, released 2 years after completion) and onshore wells from Svalbard (Senger et al., 2019). NPD's interactive FactMaps and FactPages databases were used to choose 43 offshore wells where hydrocarbons were reported in the Realgrunnen Subgroup and the data are publicly available (Fig. 1; Table 1). These discovery wells represent 33% of all exploration wells drilled on the Barents Shelf (Fig. 3B). Composite logs, well tops and press releases from NPD (2019) were used to subdivide the individual wells into eight resistivity domains using a discrete log, as illustrated in Fig. 4. These include (1) the Quaternary glacial overburden, (2) the Paleogene and Cretaceous overburden, (3) the Hekkingen Formation cap rock shale, (4) the conformably underlying Fuglen Formation (also a good seal, that in places separates the Hekkingen Formation from the underlying reservoir), (5) the Realgrunnen Subgroup siliciclastic reservoir (divided into 5) gas, (6) oil and (7) water zones according to the fluid contacts reported in NPD's FactPages) and, (8) the underlying intervals. This classification was subsequently used to quantify thickness and resistivity variation in the respective zones, as well as the depth to the reservoir. Thickness and average resistivity were combined to calculate the anomalous transverse resistance for the source rock and reservoir intervals. The average resistivity was calculated from the deep resistivity (RDEP) log using a harmonic averaging algorithm. The wireline logs were not down-sampled and from the original sampling interval of 15 cm. Obvious erroneous outliers below 0.02 Ωm and over 100 000 Ωm were removed.

Complementary geochemical data (vitrinite reflectance (VR) and T_{max} from Rock-Eval pyrolysis (McCarthy et al., 2011)) were available for

24 of the boreholes (Table 1) and were used to characterize the source rock properties. VR is a measure of the percentage of incident light reflected from vitrinite particles in sedimentary rocks. T_{max} represents the pyrolysis oven temperature at the time of maximum generation of hydrocarbons. VR and T_{max} data are only available sparingly and, in many wells, only 1–3 data points are available for the Hekkingen Formation. Only well 7120/6–1 was systematically sampled for VR and Rock-Eval. Nonetheless, we integrated all available data points along with resistivity logs to appreciate first-order trends.

In an attempt to account for lateral variations in erosion across the Barents Shelf, net erosion was averaged at each well location from five different net erosion estimates (Amantov and Fjeldskaar, 2018; Baig et al., 2016; Henriksen et al., 2011a; Ktenas et al., 2017; Lasabuda et al., 2018). Obvious outliers were removed prior to averaging. While there was an appreciable uncertainty with respect to erosion estimates, these provided a first-order link to paleo-burial depths and thus the opportunity to investigate how resistivity varies with source rock maturity and burial depth.

The resistivity measured in the boreholes was compared with CSEM-derived resistivity (vertical and horizontal) in eight wells. 1D extractions from unconstrained (i.e. no *a priori* information from seismic or well data is used) 3D anisotropic broadband inversions of CSEM data were provided by EMGS and these cover both hydrocarbon discoveries and water-bearing wells.

4. Results

4.1. Comparison of CSEM and well log resistivity

The left track in Fig. 4 illustrates the direct correlation of well log resistivity with the horizontal resistivity extracted from the unconstrained inversion of 3D CSEM data, covering the 7220/8-1 Skrugard well location. The good match between the CSEM horizontal resistivity and well data, including in the conductive interval in the water-bearing Realgrunnen Subgroup, testify to the robustness of the CSEM results. Vertical resistivity from CSEM data (Fig. 4; right track) is, on the other hand, sensitive to thin resistors and shows good correlation with the high-resistivity pay zone in the 7220/8–1 well. Note the broader response of the resistor on the CSEM data.

Recent exploration success on the Barents Shelf, including the 7324/8-1 Wisting oil discovery (38.3 mill Sm^3 recoverable resources; 241 MMboe; NPD, 2016; post-appraisal recoverable resources 440 MMboe; OMV, 2019), can be partly attributed to the use of 3D marine CSEM data integrated with 3D seismic data (Granli et al., 2017; OMV, 2019). Fig. 5A shows resistivity in three exploration wells targeting the Realgrunnen Subgroup reservoir in the Wisting area, measured both in the wells and extracted from the CSEM data (providing both horizontal and vertical resistivity). Fig. 5B shows average vertical resistivity derived from multi-client CSEM data acquired using a 3 km × 3 km receiver spacing. Reprocessing of multiclient data, and acquisition of proprietary data, which uses a tighter receiver grid (2 km × 2 km spacing) and shorter tow-line spacing, not only enabled the appraisal of the Wisting discovery but also delineation of additional resources in the near-field area (Granli et al., 2017). CSEM data assisted the successful prediction of fluid contacts and quantification of the hydrocarbon saturation prior to drilling appraisal wells (Granli et al., 2017). Discovery wells 7324/7-2 Hanssen and 7324/8-1 Wisting exhibit very high resistivity in the oil-bearing reservoir sandstones, with values exceeding 2000 Ωm. In contrast, the water-bearing Realgrunnen Subgroup reservoir in the 7324/8-2 Bjaaland well is the most conductive section of the entire well. The CSEM-derived horizontal resistivity data are in close agreement with the overall resistivity trend that increases with depth. This is most apparent in the deeper 7324/7–2 well. CSEM-derived vertical resistivity is more sensitive to thin resistors, whose lateral extent is particularly well constrained on average resistivity maps, as shown in Fig. 5B. The CSEM anomalies associated with the hydrocarbon-bearing reservoirs in the 7324/7–2 and 7324/8–1 wells are apparent in the extractions shown in Fig. 5A and the profile in Fig. 5B. The absolute resistivities in the CSEM data, which are in excess of 600 Ωm, are not as high as in the borehole, but range over a wider depth span. This is in line with the anomalous transverse resistance Baltar and Roth, 2013 (ATR) principle discussed below. In addition, note that the strongest part of the CSEM anomaly in the discovery wells does not directly correlate with the depth of the hydrocarbon-bearing interval. The vertical placement of CSEM anomalies is, in contrast to the reflective-nature of seismic data, less accurate than their lateral extent, and must be considered when interpreting CSEM data.

Fig. 6 illustrates the 7219/9-2 Kayak exploration well which targeted a Cretaceous prospect ca. 4 km down-dip from a vintage well (7219/9–1) that was found to be water-bearing in the Realgrunnen Subgroup. The 7219/9–2 well encountered 4–8 million Sm^3 of recoverable oil in Early Cretaceous sandstones and was likely drilled due to the presence of an observed CSEM anomaly (Fig. 6A). The anomaly is laterally constrained (Fig. 6B; Fanavoll et al., 2014) and follows the main structural trend in the area. In contrast to the high-quality Realgrunnen Subgroup reservoirs at Wisting illustrated in Fig. 5, the Cretaceous reservoirs of the Kolmule Formation are of moderate to poor reservoir quality. The resistivity in the well is only moderately increased in the oil zone at approximately 1500 m depth (up to 4–5 Ωm; Fig. 6C). The highest resistivity in the well is present in the lower part of the Hekkingen Formation (max 75 Ωm, average 10.8 Ωm; Table 1) with enhanced resistivity also associated with the lower part of the Kolmule Formation (3–5 Ωm). In retrospect, it is likely that the CSEM anomaly is not related to the oil-bearing zone, which exhibits a low resistivity increase compared to the background. Instead, it is likely related to other laterally constrained high-resistivity zones, for example the Hekkingen Formation. It should be noted that the Kayak discovery has a relatively long (12 km) and thin (ca. 1 km) geometry, therefore it should be expected that both pay zone resistivity and thickness to vary within the discovery.

In addition to the case studies presented above, CSEM data were used in the Barents Shelf for a variety of investigations. This includes reservoir characterization in the greater Wisting area (Alvarez et al., 2018), regional characterization of resistivity as input to revising uplift estimates away from well control (Senger et al., 2015), statistical sensitivity studies (Blixt et al., 2017) and 2D surveying over a known gas hydrate province (Goswami et al., 2017). CSEM and magnetotelluric (MT) data were also recently acquired and jointly inverted across the spreading Knipovich Ridge to the west of Svalbard (Johansen et al., 2019). Fanavoll et al. (2014) provided a pre-drill estimate of the most likely net rock volume of a Cretaceous prospect (7319/12–1 Pingvin) based on CSEM data, following the workflow presented by Baltar and Roth (2013). The applied workflow utilizes the size and strength of the CSEM anomaly, along with the site-specific CSEM sensitivity, to define the area and thickness of the hydrocarbon accumulation (i.e. net rock volume). Porosity, water saturation and recovery factors need to be assumed to convert the calculated net rock volume to producible volumes, but these can usually be constrained within a relatively narrow range. The reported post-drilling volumes were in close agreement with the published pre-drill hydrocarbon volume predictions of Fanavoll et al. (2014). This

Table 1
Discovery wells with hydrocarbons reported in the Realgrunnen Subgroup, summarizing the resistivity distribution in the Realgrunnen Subgroup and the overlying Hekkingen Formation source rock and top seal. The 7219/9-2 Kayak (Cretaceous target), 7324/8-2 Bjaaland and 7324/2-1 Apollo (both water-bearing in the Realgrunnen Subgroup) wells are included since CSEM data are available. Net erosion estimates are estimated from published net erosion maps (Henriksen et al., 2011; Baig et al., 2016; Amantov and Fjeldskaar, 2018; Ktenas et al., 2017; Lasabuda et al., 2018).

	Discovery	Water depth	Net erosion	Data availability			Source rock interval				Reservoir interval								Transverse resistance		
							Depth to Top Hekkingen	Depth to Base Hekkingen	Hekkingen Fm thickness	Hekkingen Fm average resistivity	Reservoir-Source rock separation	Depth to Top Reservoir	Gas-oil contact	Oil-water contact	Gas zone thickness	Gas zone average resistivity	Oil zone thickness	Oil zone average resistivity	Source rock only	Gas zone only	Oil zone only
		m	m	CSEM	VR	Tmax	m TVD	m TVD	m	ohm.m	m	m TVD	m TVD	m TVD	m	ohm.m	m	ohm.m	ohm.mm	ohm.mm	ohm.mm
7019/1-1	-	190	917				2321	2353	32	13.9	70	2422	2571	2571	149	316.9	-	-	443	47188	-
7119/12-3	-	211	835		*	*	2992	3072	80	5.2	37	3109	3249	3249	140	336.3	-	-	421	47031	-
7120/2-3 S	Skalle	312	1506				1974	1991	18	14.0	53	2044	2069	2069	25	25.5	-	-	251	629	-
7120/6-1	Snøhvit	314	1280		*	*	2262	2344	82	9.9	19	2363	2404	2420	41	50.2	16	22.3	810	2064	354
7120/6-2 S	Snøhvit	321	1245				2258	2334	76	8.7	13	2347	2406	2417	59	239.7	11	140.8	663	14056	1549
7120/7-1	Askeladd	233	864		*	*	2223	2365	142	6.5	18	2383	2448	2448	65	50.3	-	-	923	3272	-
7120/7-2	Askeladd	241	955			*	1995	2119	124	8.2	9	2127	2206	2206	79	60.3	-	-	1020	4743	-
7120/8-1	Askeladd	270	1247		*		1965	2061	96	6.8	6	2067	2155	2155	88	21.2	-	-	654	1870	-
7120/8-2	Askeladd	245	1179		*	*	1930	2053	123	6.6	3	2056	2136	2136	80	34.1	-	-	816	2732	-
7120/9-1	Albatross	320	1195		*	*	1790	1817	27	18.3	0	1817	1880	1880	63	54.7	-	-	494	3443	-
7120/12-2	Alke Sør	164	1198			*	1675	1850	175	4.2	13	1863	1956	1956	93	28.1	-	-	733	2618	-
7120/12-3	Alke Nord	185	1184				1922	2118	196	4.0	16	2134	2159	2159	25	27.9	-	-	778	705	-
7121/4-1	Snøhvit	335	1301		*	*	2215	2285	70	15.7	11	2296	2403	2420	107	271.5	17	41.2	1097	29083	695
7121/4-2	Snøhvit	317	1348		*	*	2315	2427	112	11.4	30	2457	2494	2494	37	40.4	-	-	1273	1495	-
7121/5-1	Snøhvit	336	1344		*	*	2269	2334	65	14.8	12	2346	2404	2419	58	24.9	15	22.4	961	1456	334
7121/5-2	Snøhvit Beta	328	1448		*	*	2235	2280	45	30.2	18	2298	2321	2334	23	75.3	13	34.8	1358	1716	453
7121/7-1	Albatross	329	1212		*		1771	1826	55	11.1	1	1827	1880	1880	53	36.3	-	-	611	1926	-
7121/7-2	Albatross	325	1198		*	*	1783	1857	74	19.3	2	1859	1892	1892	33	37.8	-	-	1427	1249	-
7121/8-1	Blåmann	376	1313				1790	1877	87	9.3	2	1879	1900	1900	21	86.2	-	-	812	1810	-
7122/6-1	Tornerose	401	1722		*		1907	1991	84	10.2	0	1991	1991	1993	-	-	2	4.1	858	-	8
7122/7-1	Goliat	381	1594				998	1064	66	6.1	14	1078	1078	1122	-	-	44	47.7	401	-	2099
7122/7-2	Goliat	377	1578				1003	1049	46	8.8	11	1060	1060	1136	-	-	76	64.4	405	-	4892
7122/7-3	Goliat	343	1605		*	*	993	1048	55	8.3	14	1062	1121	1125	59	229.2	4	176.7	454	13531	707
7122/7-6	Goliat	380	1614				1012	1076	64	6.2	11	1087	1087	1128	-	-	41	141.7	396		5808
7124/3-1	Bamse	273	1405		*	*	1210	1261	51	3.2	0	1261	1274	1275	13	13.5	1	3.6	164	173	4
7125/1-1	Binne	252	1409		*	*	1320	1375	55	4.1	0	1375	1380	1381	5	2.1	1	6.7	225	10	7
7125/4-1	Nucula	293	1415			*	794	846	52	2.3	3	849	871	916	22	6.6	45	5.4	120	146	243
7125/4-2	Nucula	294	1432				868	907	39	3.5	0	907	907	923	-	-	16	5.3	138	-	84
7219/8-2	Iskrystall	344	957				2754	2763	9	8.5	99	2862	3096	3096	235	86.2	0	-	76	20208	-
7219/9-2	‡Kayak	336	1068	*			2230	2396	166	10.8	160	2556	-	-	-	-	-	-	-	-	-
7219/12-1	Filicudi	323	1269				1499	1501	2	109.2	2	1503	1576	1632	73	216.2	56	91.3	218	15782	5111
7220/2-1	Isfjell	429	1603				-	-	0	-	-	828	872	874	44	98.5	2	6.4	-	4336	13
7220/4-1	Kramsnø	403	1381				-	-	0	-	-	2267	2369	2369	102	109.7	-	-	-	11185	-
7220/5-1	Skrugard	388	1314				1256	1272	16	2.7	25	1297	1325	1372	28	20.7	47	35.8	43	581	1681
7220/7-1	Havis	365	1270	*			-	-	0	-	-	1741	1788	1916	47	487.3	128	580.9	-	23003	74352
7220/7-2 S	Skavl	349	1424				-	-	0	-	-	1062	1089	1112	27	34.7	23	50.9	-	932	1170
7220/8-1	Skrugard	374	1285	*			-	-	0	-	-	1252	1288	1371	36	244.0	83	566.3	-	8733	47002
7220/10-1	Salina	348	1447				1450	1465	15	2.7	15	1479	1533	1533	54	30.9	-	-	41	1655	-
7225/3-1	Norvarg	377	2005				631	656	25	4.1	31	687	727	727	40	88.8	-	-	101	3555	-
7324/2-1	†Apollo	444	2269	*			755	757	2	5.4	92	849	-	-	-	-	-	-	11	-	-
7324/7-2	Hanssen	418	2260	*			590	626	36	8.2	46	672	672	692	-	-	20	1781.0	295	-	35620
7324/8-1	Wisting	424	2208	*	*		590	621	31	6.2	41	662	662	708	-	-	46	12372.0	192	-	569112
7324/8-2	†Bjaaland	394	2136	*			613	632	19	5.6	36	668	-	-	-	-	-	-	106	-	-
7324/9-1	Mercury	414	2094				631	635	4	86.1	21	656	666	666	10	2512.5	-	-	345	25125	-
7325/4-1	Gemini	447	2051	*			692	732	40	7.0	40	772	790.5	790.5	19	341.8	-	-	280	6323	-

† Two water-wet exploration wells are included in this study to compare the CSEM response to resistivity measured in the borehole
‡ The 7219/9-2 Kayak well targeted a shallower structure than the Realgrunnen Subgroup (which was water-bearing in the well) but is included due to the available CSEM data
Bold wells are related to currently producing fields (Snøhvit area, Goliat) or fields in development phase (Johan Castberg, first oil in 2022). In addition, several other discoveries including Wisting are classified as "production in clarification stage" (NPD)

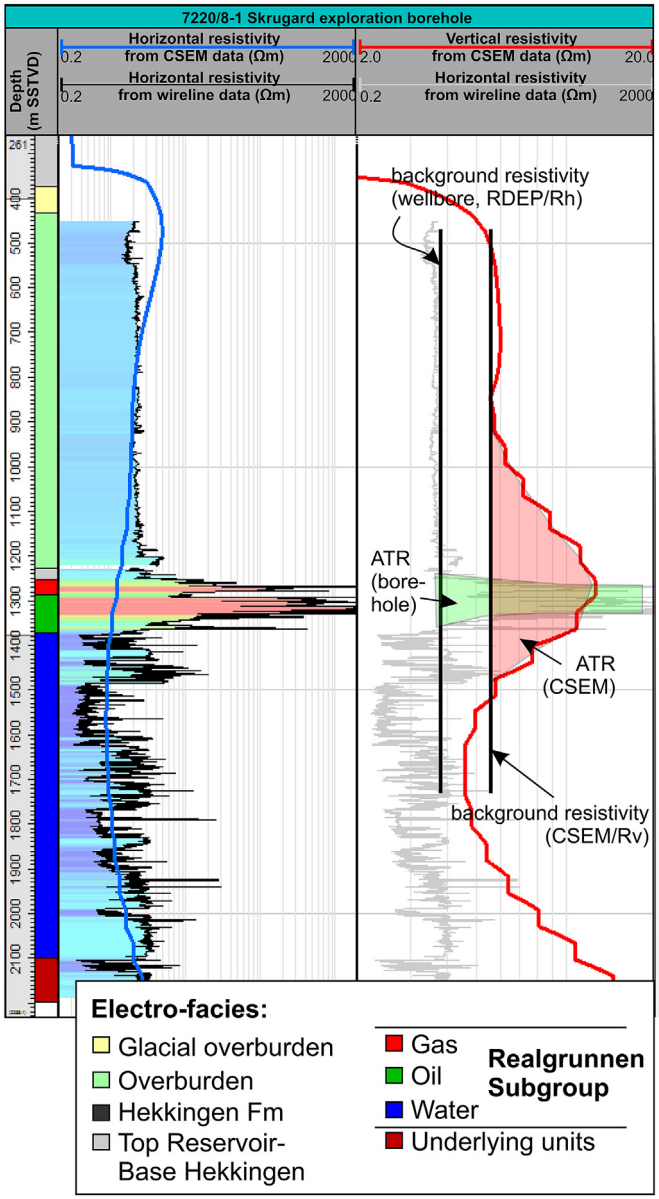

Fig. 4. Overview of horizontal resistivity (R_h) variation with depth as measured with a standard deep resistivity logging tool in the 7220/8-1 Skrugard discovery well, illustrating the subdivision of the electrofacies applied in this study. The subdivision is based on formation tops and fluid contacts reported in NPD's FactPages. The concept of anomalous transverse resistance (ATR) is illustrated on the second track, with the well log resistivity (green) and the CSEM resistivity (red) ATR.

illustrates that the CSEM anomaly only covered the up-dip section of a much larger seismic-amplitude driven prospect.

4.2. Organic rich shale vs reservoir sandstones

The Hekkingen Formation is present in 38 of the 43 investigated discovery wells (Table 1), and ranges from 2 m (7219/12–1) to 196 m (7120/12–3) in thickness, with an average thickness of 57 m. The Realgrunnen Subgroup is hydrocarbon-bearing in all investigated wells (Table 1), with gas present in 34 of 43 wells and oil in 22 of 43 wells. Table 1 summarizes the thickness and average resistivity of the Hekkingen Formation and the hydrocarbon-bearing Realgrunnen Subgroup. Table 1 also provides the calculated transverse resistance of the units (TR = thickness × resistivity).

Resistivity variation is illustrated in Fig. 7. The majority of the Hekkingen Formation has a mean resistivity of approximately 10 Ωm, while the mean resistivity of the gas and oil-bearing Realgrunnen intervals is typically 1–2 orders of magnitude higher. The heterogeneity is significantly larger in the Realgrunnen Subgroup hydrocarbon-bearing zones than it is in the Hekkingen Formation. All of the investigated wells are merged in Fig. 8, illustrating that the Hekkingen Formation has a clearly defined peak with a P50 average of 5.3 Ωm. The oil- and gas-bearing reservoir zones display considerably more variability. Nonetheless, they both offer significantly higher P50 averages (oil = 21.9 Ωm, gas = 35.2 Ωm) than the Hekkingen Formation. Furthermore, resistivity discriminates the hydrocarbon-bearing intervals within the Realgrunnen Subgroup from the water-bearing zones (P50 average = 3.6 Ωm). Deep burial and cementation will serve to enhance the resistivity of a reservoir, but this increase is significantly lower than the resistivity increase associated with high hydrocarbon saturation.

4.3. Resistivity in organic rich-shales as a function of maturation and organic richness

Fig. 9 illustrates a regional profile from the Hammerfest Basin to the northern Barents Shelf. This profile specifically focuses wells where vitrinite reflectance (VR, Ro%) and Tmax data from drill cuttings are available for the Hekkingen Formation. At such regional scale there clearly is major variation in both thickness and maturity of the Hekkingen Formation, including the Hammerfest Basin. Two wells in the Hammerfest Basin (7120/6–1 and 7121/5–2) fall in the oil window for the Hekkingen Formation depth interval using both maturity indicators. The Hekkingen Formation in well 7120/8–2 is in the immature window in four out of five samples, likely reflecting that it is shallower than the other two wells. The resistivity logs are, in general, similar between the three wells, displaying enhanced resistivity in the lower part of the Hekkingen Formation. This shift is also apparent in the gamma ray log and is attributed to lithological variations. The highest resistivity, locally exceeding 100 Ωm, is evident in the 7121/5–2 well. To quantify the effect of source rock maturity on the resistivity, VR and T_{max} are plotted as functions of both present-day and net erosion corrected depths (Fig. 10). There is an overall correlation with increasing maturity with increasing depth, covering a relatively large interval from 500 to 3100 m in present-day depth. When correction factors are applied, this trend is even more evident. T_{max} data are limited, but suggest a positive correlation with increasing burial depth when a certain threshold of burial is exceeded (ca. 2500 m in Fig. 10). The resistivity logged in the Hekkingen Formation in the same wells exhibits a similar trend, in general increasing with depth (Fig. 10). The internal variation of the Hekkingen Formation resistivity is nonetheless higher than this trend that increases from ca. 2 Ωm at 800 m to ca. 5 Ωm at 3000 m depth. Interestingly, the wells with the highest resistivities (40–100 Ωm) all cluster in a relatively narrow "paleo-depth" range from 2200 to 3600 m. The Hekkingen Formation exhibits lower resistivity both above and below this window, which is likely related to the source rock being immature or, conversely, overcooked.

Direct correlation of resistivity with VR (Fig. 11) suggests a positive correlation with increasing resistivity in increasingly mature source rocks. In the investigated wells the resistivity does not exceed 110 Ωm and, as illustrated in Fig. 10, the resistivity tends to decrease again in wells where the Hekkingen Formation is deeply buried. This is presumably related to over-maturation of the unit.

Passey et al. (1990) present the sonic-resistivity overlay (i.e. Δ log R method) to quantify total organic content (TOC) using wireline data. There is a very good correlation between TOC and resistivity in DH5R, a research well in Svalbard characterized in detail by Koevoets et al. (2019), and in some of the offshore wells as illustrated by 7219/8-1 S (Fig. 12). TOC data from Rock-Eval pyrolysis on selected wells indicate a

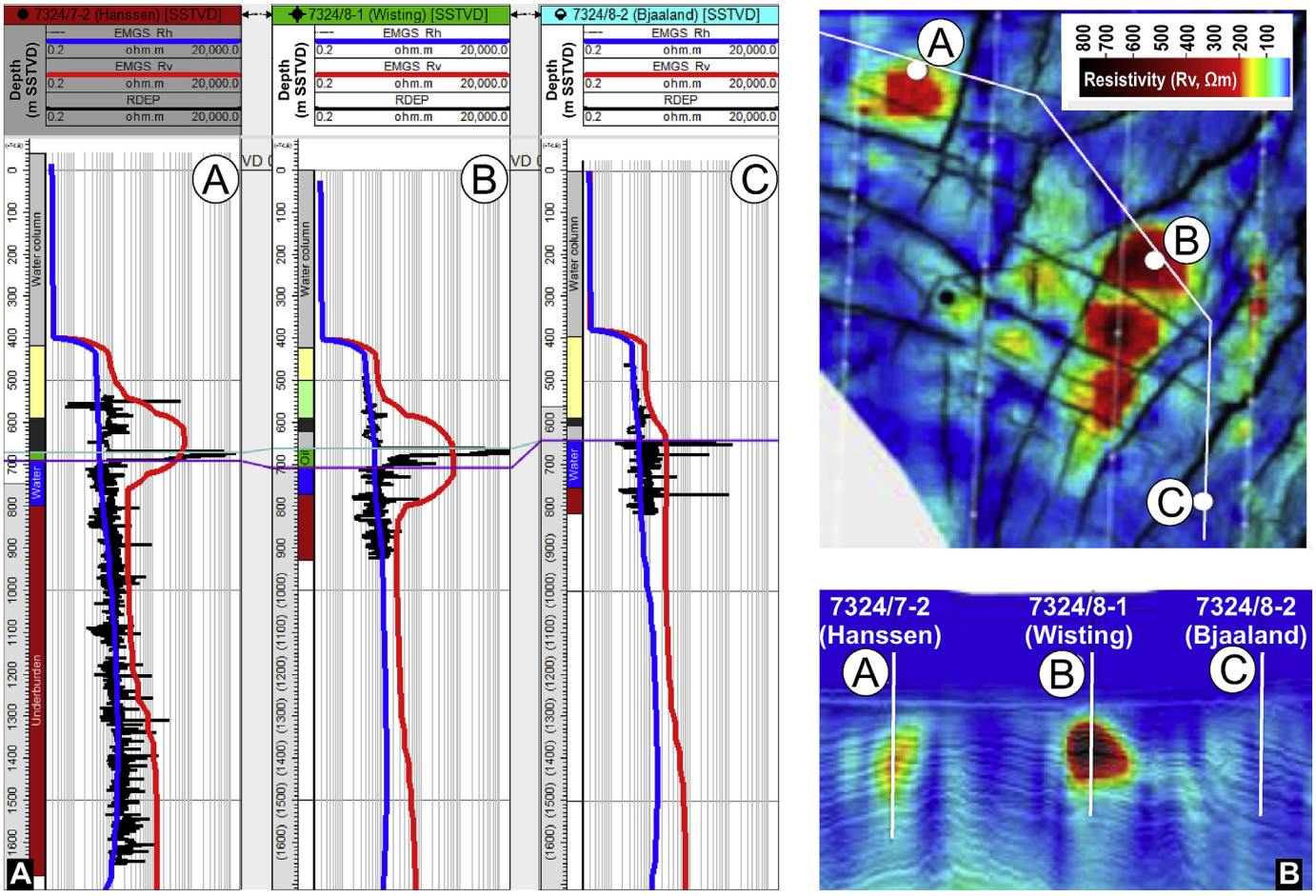

Fig. 5. Comparison of CSEM data and well-measured resistivities in the Wisting area. (A) Well logs and CSEM-data extractions at three well locations, including the Hanssen and Wisting discoveries, and the Bjaaland water-wet well. (B) The map shows average vertical resistivity, while the composite profile illustrates the CSEM data along with seismic data, map and profile from Granli et al. (2017).

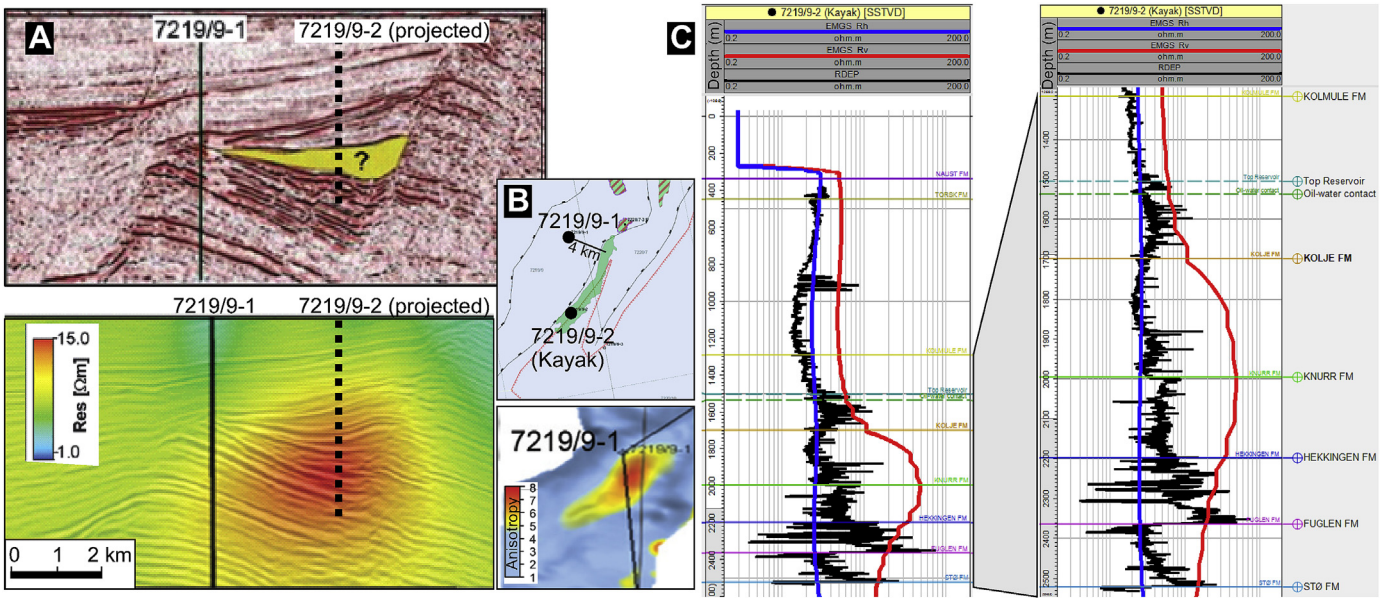

Fig. 6. Example of a CSEM-driven prospect, 7219/9-2 Kayak, that was drilled in 2017 and proved 4–8 million Sm^3 of recoverable oil in syn-rift Cretaceous strata. (A) Seismic and CSEM vertical resistivity over the Kayak prospect, published prior to drilling by Fanavoll et al. (2014). (B) Outline and dimensions of the Kayak discovery and relationship between the two discussed wells, from NPD FactMap. The lower inset shows an extract from a regional map of electrical anisotropy, published by Fanavoll et al. (2014). (C) Deep resistivity log from the 7219/9-2 borehole, overlain with CSEM-data extractions of horizontal (blue) and vertical (red) resistivity. The zone of interest is zoomed-in on the right size. Note the large difference in the resistivity scale compared to Wisting shown in Fig. 5.

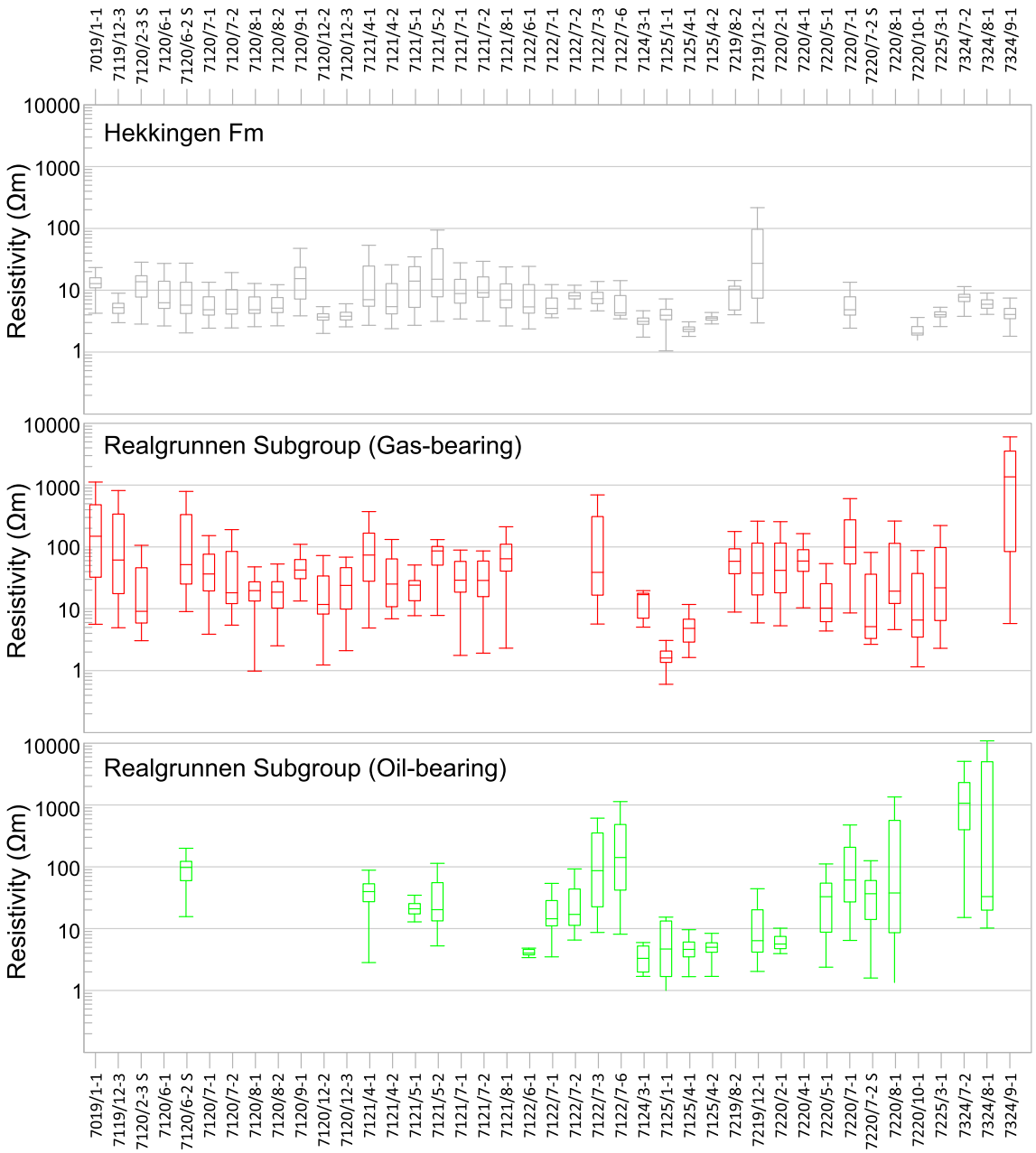

Fig. 7. Resistivity variation in the different electro-facies grouped well by well. Overview of the horizontal resistivity measured in selected hydrocarbon-bearing wells in the Barents Sea, subdivided into electro-facies representing the overburden, the organic-rich Hekkingen Formation cap rock and the gas and oil zones. The box-whisker plots provide a quick overview of the statistical distribution of the measured resistivity in each interval, plotting maximum, minimum, mean and the upper and lower quartiles.

very convincing trend towards low velocity, high resistivity, high gamma ray and high TOC source rock populations (Fig. 13).

5. Discussion

5.1. Resistivity controls in reservoir sandstones

The hydrocarbon bearing zones, subdivided into gas and oil zones based on the reported fluid contacts (Fig. 4), show the largest variation in resistivity spanning several orders of magnitude from 0.3 to >20 000 Ωm (Fig. 7; Table 1). This is controlled primarily by reservoir quality and water saturation. Since Archie (1942) proposed an empirical relationship linking porosity, water saturation and cementation, countless publications have used or developed Archie's law to quantify the water saturation in the pay zone (e.g., Worthington, 1993 and references therein). This was motivated to quantify water saturation in low-resistivity pay zones (Worthington, 2000), which can easily be overlooked when only traditional water saturation estimates are attempted. A wide range of factors affecting pay zone resistivity exists that includes shale content (Revil et al., 1998; Worthington, 1982), pore throat radius (Ziarani and Aguilera, 2012), cementation (Salem and Chilingarian, 1999), temperature (Sen and Goode, 1992), salinity (Cameron et al., 1981; Worthington, 1993) and the presence of electrically conductive minerals such as pyrite or graphite (Pridmore and Shuey, 1976; Spacapan et al., 2019). Rock physics work using electrical measurements is vastly under-represented in the literature when

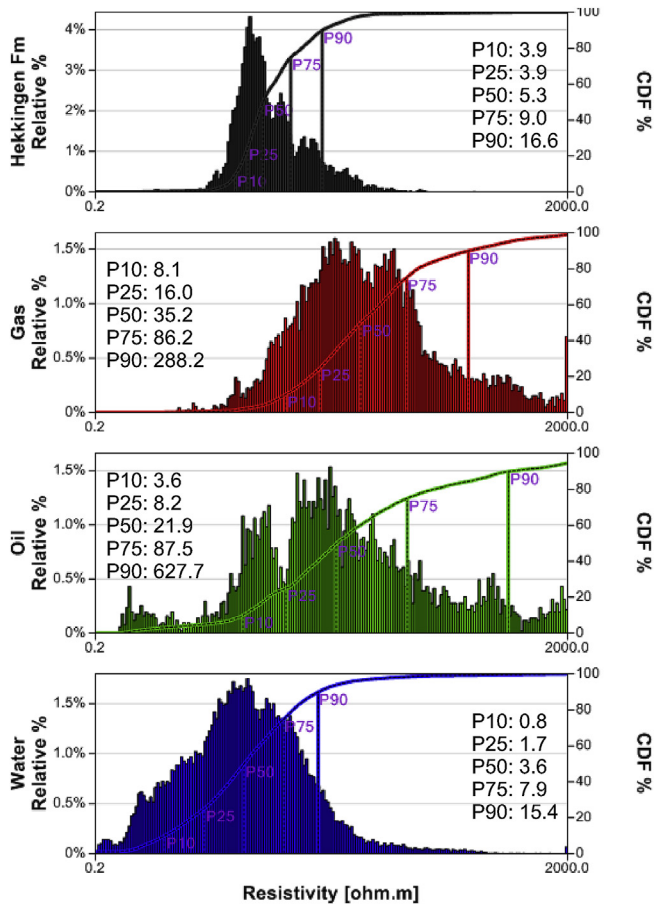

Fig. 8. Histograms illustrating the resistivity measured in the 43 investigated hydrocarbon bearing wells, with corresponding probability functions for the Hekkingen Formation, gas and oil zones. CDF = cumulative distribution function.

compared with elastic parameters. Exceptions include studies on cross-property relationships between velocity and resistivity (Carcione et al., 2007), useable, for instance, for generating improved velocity models for seismic inversion (Werthmüller et al., 2013), production-related changes on resistivity (Gelius and Wang, 2008), electrical anisotropy (Ellis et al., 2010a) and joint simulations of electric and elastic parameters (Aquino-López et al., 2011). More recently, the increased use of CSEM data motivated laboratory-based studies correlating low-frequency (2 Hz) resistivity with porosity, clay content and permeability in reservoir sandstones (Han et al., 2015).

Fig. 14 illustrates the saturation effect on resistivity in two nearby (9.5 km apart) wells on the Polheim sub-platform. While the hydrocarbon-bearing 7220/7-1 discovery offers extremely high resistivities (6.4–22,314 Ωm, average 580.9 Ωm), particularly in the oil section with best reservoir properties, the 7219/9-1 borehole is water-bearing in the Realgrunnen Subgroup. The very low resistivity reflects the contribution of electrically conductive brine and is considered as analogous to the water leg in the 7220/7-1 discovery. Note, however, that in well 7220/5–2 there is strong resistivity variation within the hydrocarbon bearing zone, probably reflecting vertical variation in porosity, shale content, water saturation, cementation and fracturing (Senger et al., 2017a). Interestingly, the pay zone resistivity is lower in the gas zone than in the oil zone in the 7220/7–1 well, which is attributed to poorer reservoir quality in the upper part of the Realgrunnen Subgroup. The gamma ray log in Fig. 7 likely indicates an organic rich intra-formational seal or baffle in the lower part of the gas-bearing interval, with decreasing shale content upwards.

5.2. Resistivity controls in organic rich shales

Resistivity in organic rich shales is governed by both matrix and fluid effects, and is amongst others sensitive to porosity, organic richness, kerogen type and content, presence of solid bitumen and maturation level (e.g., Kethireddy et al., 2014; Rudnicki, 2016; Zhao et al., 2007). In contrast to reservoir sandstones where conventional resistivity -porosity-saturation models are routinely used, the characterization of shales is complicated by the presence of electrically conductive kerogen and conductive minerals such as pyrite.

During thermal maturation, organic matter is eventually transferred to graphite, leading to low electrical resistivity measurements in highly mature zones of source rocks. Yang et al. (2016) confirmed this phenomenon by measuring electrical resistivity of kerogen in Haynesville and Eagle Ford shale samples at a range of controlled maturity levels. They show that thermal maturation initially (up to 300°C) severely increases resistivity of the shale as free and absorbed water molecules are lost as petroleum is generated. At later stages (300–800°C), resistivity decreases, which is attributed to extensive graphitization and an increase in the aromaticity of the kerogen.

The Hekkingen Formation displays considerable variability in measured resistivity, presumably related to the level of maturity, organic richness, lithology, and fracturing. In most wells the resistivity is below 10 Ωm (Fig. 7). The 7219/12–1 well offers the highest mean resistivity (109 Ωm), but the Hekkingen Formation is extremely thin in this borehole (2 m; Table 1). Clearly, there is a bias in that most exploration wells are drilled on structural highs and not deep in basins where source rock intervals are likely to be thicker and more resistive due to active hydrocarbon generation. On the Barents Shelf many wells provide evidence that hydrocarbon generation has occurred prior to Cenozoic uplift.

In this context, laboratory-derived resistivities of samples of Posidonia black shales from the Lower Saxony Basin in Germany, at various stages of maturity, by Adão et al. (2016) is of great importance. Adão et al. (2016) measured the resistivity of 14 samples ranging in maturity from immature (0.53% Ro) to gas window (1.45% Ro) in both dry state and when using distilled water. All samples were resistive with values exceeding 100 Ωm. Increased TOC typically gives higher resistivity (for the dry samples) although the TOC range is relatively minimal for the immature stage. Porosity has a strong influence on the resistivity of the samples, suggesting that the resistivity is primarily controlled by the presence of the electrically conductive brine. Interestingly, there was no correlation between resistivity and thermal maturity in the investigated samples (Adão et al., 2016).

5.3. CSEM and well-derived resistivity: similarities and differences

Resistivity is measured at a range of scales, directions and frequencies, and robust upscaling and downscaling methods are required to relate CSEM-derived resistivity to well-logged resistivity (Løseth et al., 2014; Olsen, 2011). Baltar and Roth (2013) introduced the concept of anomalous transverse resistance (ATR). ATR is a thickness-resistivity product that describes the cumulative resistivity contrast in hydrocarbon-bearing reservoirs, against an average background resistivity trend (Fig. 4). ATR can thus be used to predict true pay zone resistivity from CSEM data, given that the net reservoir thickness is known or assumed, and is therefore a critical component of pre-drill volumetric assessments (e.g., Baltar and Barker, 2015). ATR is applicable when a 1D earth model is considered, without considering 2D or 3D

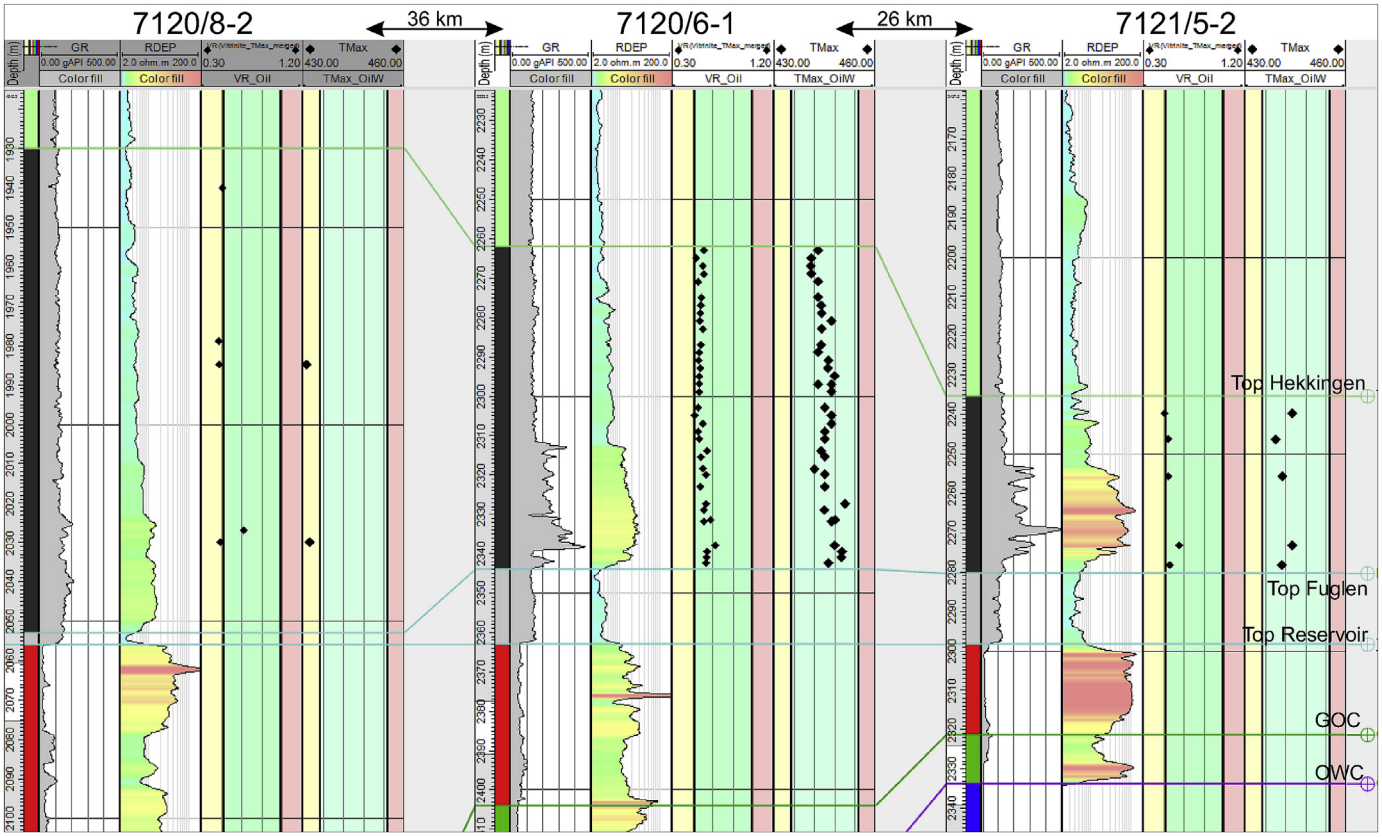

Fig. 9. Well correlation across selected wells showing vitrinite reflectance and T_{max} with gamma ray and resistivity logs. The correlation also illustrates the thickness variation of the Hekkingen Formation (black part of discrete log). The oil window maturity ranges are 0.5–1.0 (R_o) and 435–455 °C (T_{max}).

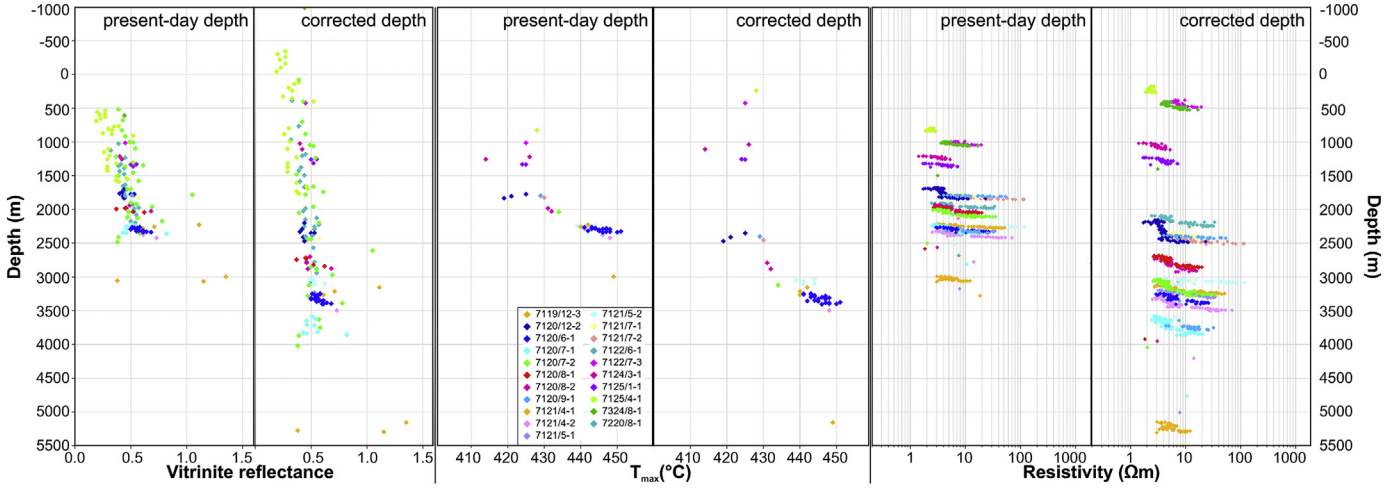

Fig. 10. Comparison of resistivity measured in boreholes with source rock maturity, as provided by vitrinite reflectance (VR, %Ro) and T_{max} measurements on the Hekkingen Formation. The data are plotted in both present-day depth, and in corrected depth reflecting the variable net erosion across the Barents Shelf. The correction net erosion factors are listed in Table 1, and are based on a number of published erosion maps (Henriksen et al., 2011; Baig et al., 2016; Amantov and Fjeldskaar, 2017; Ktenas et al., 2017; Lasabuda et al., 2018).

effects. In the context of stacked reservoirs, or hydrocarbon-bearing sandstones overlain by resistive organic rich shales, the ATR equivalence principle can be applied to quantify the relative contribution of the two resistors. In addition, resistivity is a highly anisotropic and scale-dependent parameter, with electrical conduction varying significantly with the direction and scale of the measurement. Electrical anisotropy is defined as R_v/R_h, where R_v = vertical resistivity and R_h = horizontal resistivity. Electrical anisotropy is measurable at core

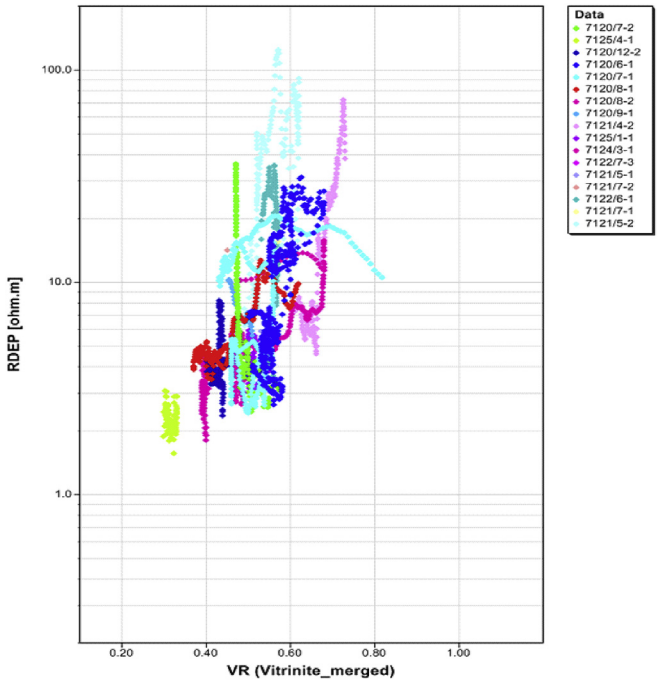

Fig. 11. Correlation between resistivity logs and vitrinite reflectance (VR) in the Hekkingen Formation, color-coded by wells.

plug-scale in the lab (North et al., 2013; North and Best, 2014), to well-scale (Ellis et al., 2010a, 2010b; Moran and Gianzero, 1979) to CSEM-scale (Løseth et al., 2014; Newman et al., 2010). Modern 3D CSEM inversion is anisotropic, while most vertical exploration boreholes are primarily sensitive to horizontal resistivity. Boreholes equipped with tri-axial resistivity tools able to derive the vertical resistivity are rare (e.g., Clavaud, 2008), particularly in non-reservoir sections. Nonetheless, several wells in the Barents Sea have acquired tri-axial data in the overburden section (Vereshagin et al., 2019). This has been performed partly to assist in interpreting CSEM data (Løseth et al., 2014) and to constrain the effects of electrical anisotropy in the Barents Sea (Ellis et al., 2017; Schneider et al., 2015; Vereshagin et al., 2019; Wedberg et al., 2017). The scale of measurement also controls anisotropy; therefore anisotropy at well-scale cannot be compared to anisotropy at CSEM-scale. Scaling effects from well to CSEM-scale must also be considered to accurately represent small-scale variability at the well scale on the coarser CSEM-scale (Olsen, 2011).

5.4. *Implications for CSEM interpretation: applicability and limitations*

Our objective is to quantify the resistivity variation within the Hekkingen Formation compared to the underlying hydrocarbon-bearing reservoirs of the Realgrunnen Subgroup in the context of CSEM interpretation. As such, it is necessary to consider the transverse resistance

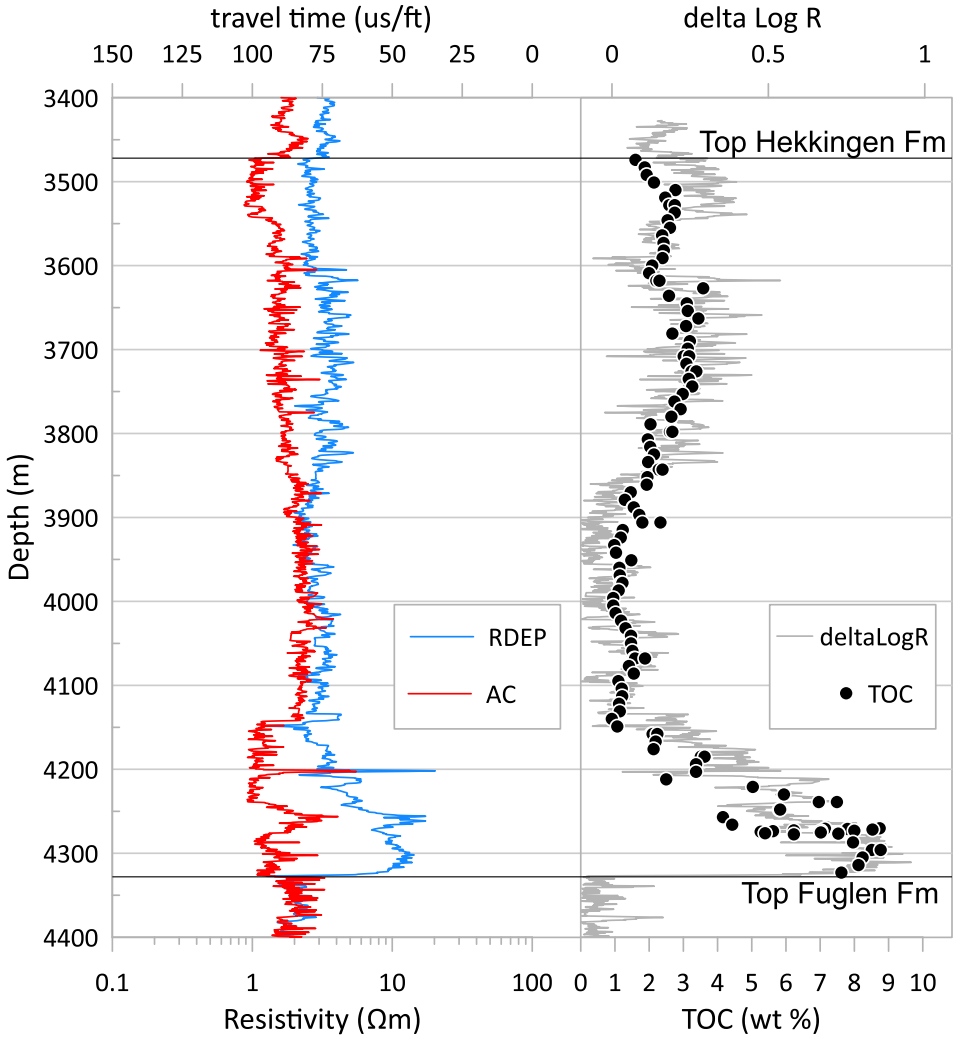

Fig. 12. Resistivity-sonic overlay of the 7219/8-1 S borehole. $R_{baseline}$ = 2 Ωm, $\Delta t_{baseline}$ = 80 us/ft.

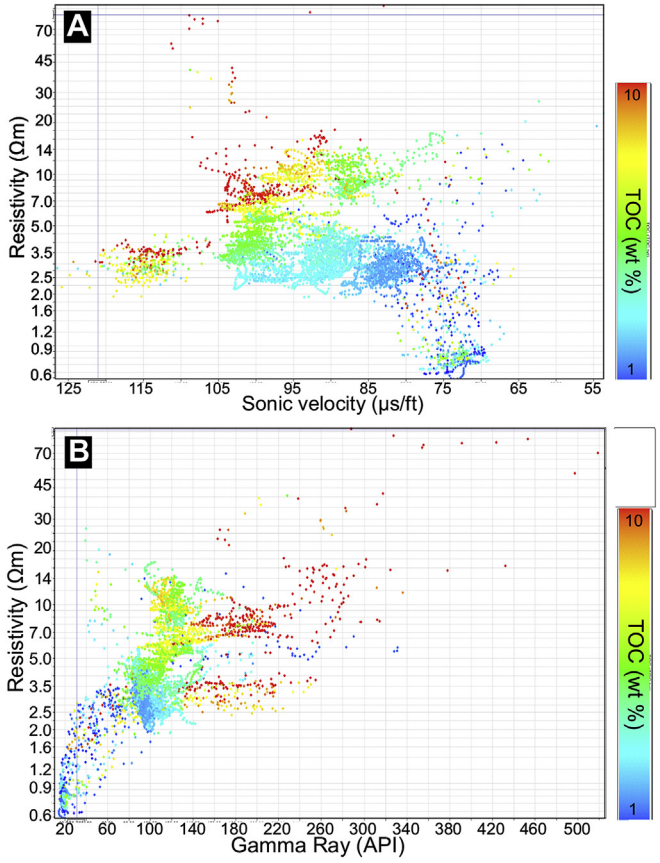

Fig. 13. Resistivity variation in the organic rich shales of the Hekkingen Formation. (A) Resistivity versus sonic of the Hekkingen Formation, color-coded by TOC content measured in cuttings. (B) Cross-plot of resistivity vs. gamma ray, color-coded by TOC content measured in cuttings. Only wells where TOC data is measured in drill cores or cuttings are used, namely 7120/1–2.7120/12–1, 7122/2–1, 7219/8-1 S, 7321/9–1, 7124/3–1, 7120/2-2, 7226/11–1, 7324/7-1 S and DH5R.

(TR) of the different units as illustrated in Fig. 15 and listed in Table 1. The Hekkingen Formation typically exhibits TR values from 100 to 1000 Ω m^2, while the hydrocarbon-bearing zones usually exceed 1000 Ω m^2, in some cases by two orders of magnitude. With comparable zone thicknesses of the hydrocarbon columns and Hekkingen Formation thickness it is primarily the average zone resistivity that determines the TR of the units.

As with other geophysical methods, CSEM has its limitations and uncertainties that must be evaluated to prevent interpretation pitfalls. Most importantly, CSEM data image subsurface resistivity. Thus, it is the responsibility of the explorationists to evaluate the significance of any enhanced subsurface resistivity with respect to possible hydrocarbons, or other resistivity-enhancing features. Integration with other data, in particular seismic, is crucial for the interpretation of CSEM data (e.g., Fanavoll et al., 2014; Tharimela et al., 2019). In addition, the interpreters must be aware that there is some uncertainty in the vertical placement of CSEM anomalies, which can be quantified through scenario testing using CSEM forward modelling. On the other hand, the lateral placement of CSEM anomalies is very good when 3D CSEM data are used, and can be used, for instance, to predict fluid contacts prior to drilling (Granli et al., 2017). Finally, geological complexity and increasing depth decrease the

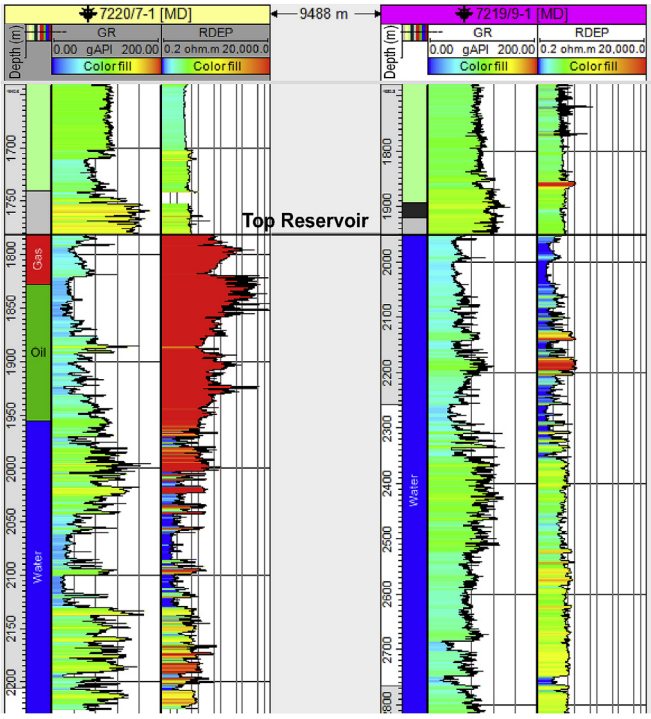

Fig. 14. Well correlation across a hydrocarbon-bearing well 7220/7–1 and a water-bearing well 7219/9–1, flattened on top reservoir.

CSEM sensitivity, which must be accounted for when interpreting CSEM data.

Fig. 16 illustrates the CSEM response from five hydrocarbon-bearing discoveries and two water-bearing wells, all targeting the Realgrunnen Subgroup reservoir. The two water-bearing wells, 7324/2-1 Apollo and 7324/8-2 Bjaaland, are both located near Wisting, where the target reservoir is extremely shallow (200–250 m beneath the seafloor). From a CSEM-perspective, these shallow targets have extremely high sensitivity. Therefore, the lack of CSEM anomalies in both of these structures was attributed to water-bearing, residual or low-saturation hydrocarbon-bearing reservoirs prior to drilling. The resistivity log from the drilled wells confirms the CSEM predictions, with conductive brine-bearing reservoirs. The high background resistivity may "hide" some low-to moderate-saturation reservoirs, but it is notable that even minor hydrocarbon accumulations are imaged by CSEM data in the area. A good example of this is the 7325/4–1 Gemini gas discovery, located north-east of Wisting, which demonstrates a strong CSEM anomaly corresponding to increased resistivity within a 19 m thick gas column in the Realgrunnen Subgroup (Fig. 16). The operator reports 0.4 to 1 billion Sm^3 of recoverable gas, stating also that the discovery is not profitable as of today. In other words, within this area of very high CSEM sensitivity, CSEM data can detect even small gas accumulations below 1 billion Sm^3, suggesting that CSEM data should be considered as a tool for de-risking. The strength of the CSEM anomaly increases with both pay zone resistivity and pay zone thickness, well exemplified by the 7324/7-2 Hanssen and 7324/8-1 Wisting wells (Figs. 5 and 16).

Further south in the Barents Sea, the Realgrunnen Subgroup is located deeper, at 900–1400 m below seafloor. Well log resistivity and reported fluid contacts indicate a thicker pay zone in both the 7220/8-1 Skrugard and 7220/7-1 Havis discovery wells (both now part of Johan Castberg field development). The extracted CSEM anomalies are not as strong as in

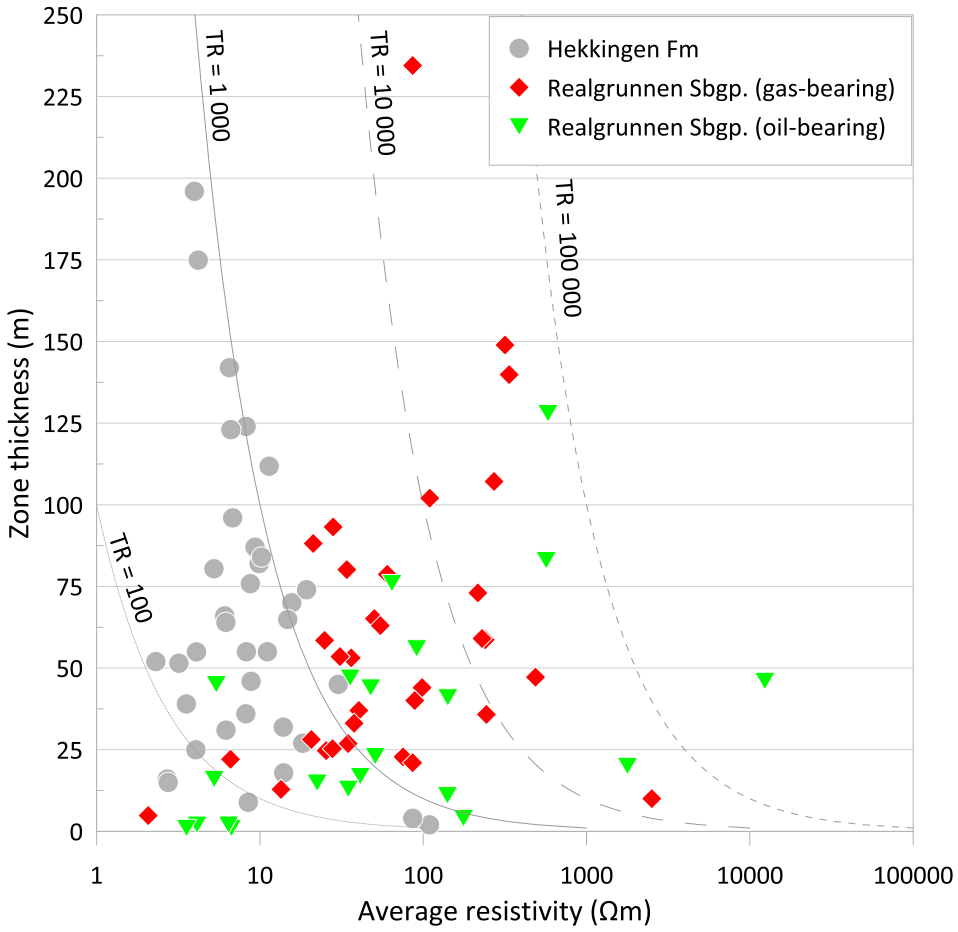

Fig. 15. Average resistivity versus zone thickness, color-coded by fluid phase in Realgrunnen Subgroup and the Hekkingen Fm. The transverse resistance (TR) lines illustrate the theoretical equal sensitivity of CSEM data to a resistor's thickness×resistivity product. Table 1 provides details on the input data.

the ultra-shallow reservoirs around Wisting. Here, increased sub-seabed depth to reservoir interval results in a decrease in CSEM sensitivity. Nonetheless, both wells (7220/7-1 Havis in particular) exhibit constrained vertical resistivity anomalies. Their lateral extent has been previously shown to be constrained, and in agreement with the seismically-mapped structures (Fanavoll et al., 2014; Gabrielsen et al., 2013).

6. Conclusions

In this contribution we have investigated the resistivity variation as measured in exploration boreholes in the Barents Shelf, focusing on the resistivity variation in reservoir sandstones and the overlying cap rock shales. We conclude that:

(1) Resistivity in organic rich shales, in particular the Upper Jurassic–Lower Cretaceous Hekkingen Formation source rock, is a function of both the total organic content and its maturation stage. In the investigated wells, mean resistivity in the Hekkingen Formation does not exceed 109 Ωm.
(2) The hydrocarbon bearing Realgrunnen Subgroup sandstones exhibit extremely high resistivity in excess of several hundred to thousands Ωm. This is especially valid in fields and discoveries currently considered as commercial. In smaller discoveries where development is considered unlikely (i.e. sub-commercial), the pay zone resistivity is often less than 100 Ωm.
(3) We have particularly focused on parameters relevant for exploration away from well control where factors such as a resistor's transverse resistance (i.e., thickness X resistivity), its sub-seafloor depth and vertical separation to other resistors are all important when interpreting controlled-source electromagnetic data. As such, this study presents a framework for interpreting resistivity data away from wells, such as CSEM or MT data sets.
(4) In organic rich shales, resistivity generally increases with increasing maturity towards a depth-dependent threshold, from which it decreases again towards over-mature source rocks.
(5) CSEM data are in very good agreement with resistivity measured in wellbores, particularly in areas of high CSEM sensitivity such as the shallow Realgrunnen Subgroup reservoirs in the northern part of the Barents Shelf.
(6) The transverse resistance of the encountered Hekkingen Formation shales is found to be below 1000 Ωm^2 in all wells. In contrast, transverse resistance in hydrocarbon-bearing reservoirs within the Realgrunnen Subgroup in most cases exceeds the 1000 Ωm^2 threshold.

Declaration of competing interest

The authors declare that they have no known competing financial

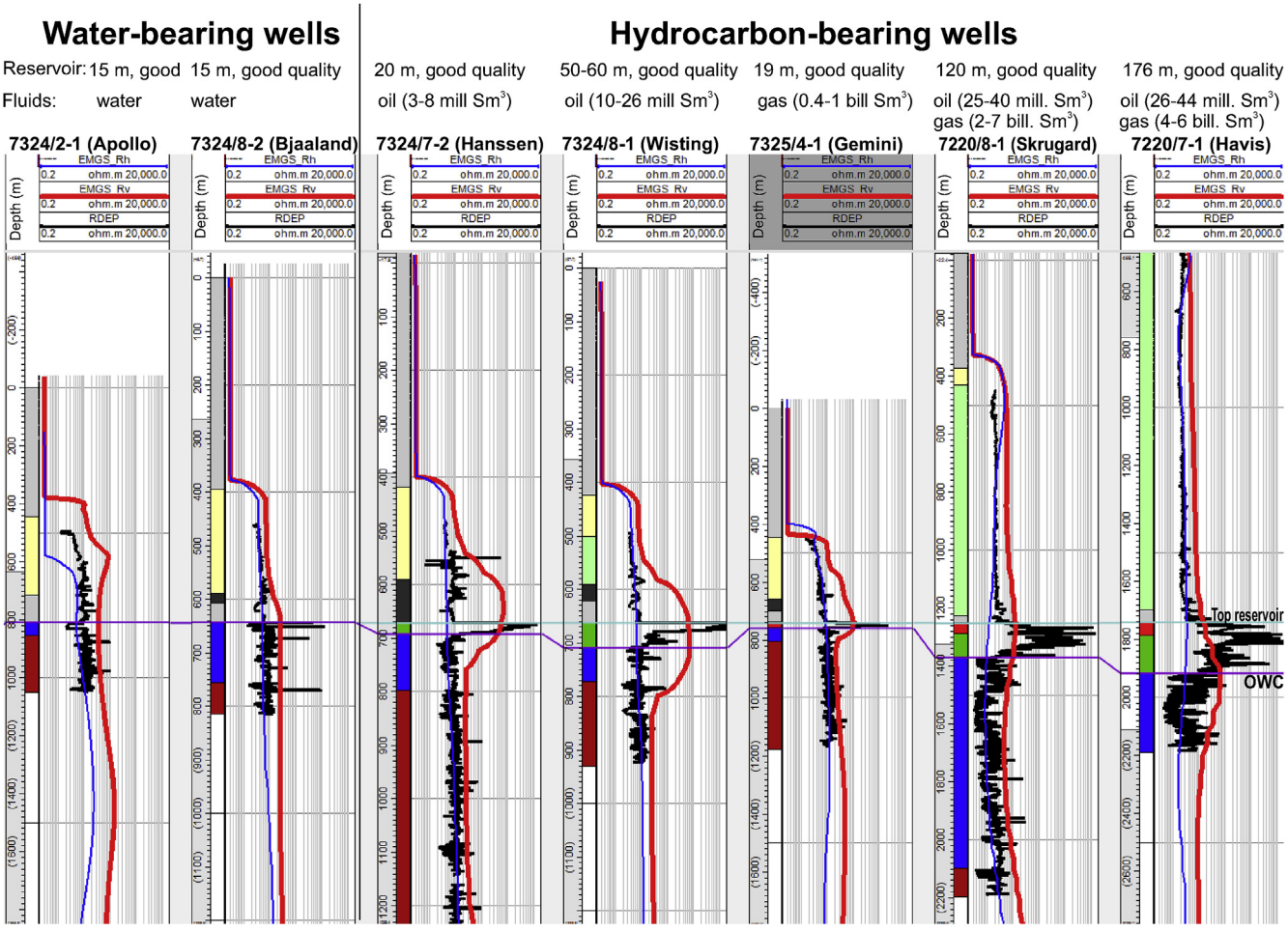

Fig. 16. Overview of the resistivity response from borehole measurements and CSEM data for two water-bearing wells and five hydrocarbon-bearing wells. The well correlation panel is flattened on the top of the Realgrunnen Subgroup reservoir, targeted by all wells. The reported volumes are from NPD (2019).

interests or personal relationships that could have appeared to influence the work reported in this paper.

Acknowledgements

This research is funded by the Research Centre for Arctic Petroleum Exploration, supported by industry partners and the Research Council of Norway (Grant No. 228107). PB was partly financed by the Norwegian CCS Centre, financed by the Research Council of Norway (Grant No. 257579) and industry partners. We sincerely appreciate the generous data access, particularly from the Norwegian Petroleum Directorate (DISKOS database, NPD FactPages and Svalbard exploration boreholes) and the UNIS CO_2 lab (http://co2-ccs.unis.no) for access to the CO_2 research boreholes onshore Svalbard. EMGS kindly provided CSEM data at eight well locations. Amando Lasabuda kindly provided digital versions of published net erosion maps. UNIS acknowledges the academic licenses of Petrel and the Blueback Toolbox generously provided by Schlumberger and Cegal, respectively. Finally, we are grateful to two anonymous journal reviewers for their constructive feedback, and Gareth Lord for proof-reading the manuscript.

References

Abay, T.B., Karlsen, D.A., Pedersen, J.H., Olaussen, S., Backer-Owe, K., 2018. Thermal maturity, hydrocarbon potential and kerogen type of some Triassic–Lower Cretaceous sediments from the SW Barents Sea and Svalbard. Petrol. Geosci. 24 (3), 349–373.

Adão, F., Ritter, O., Spangenberg, E., 2016. The electrical conductivity of Posidonia black shales—from magnetotelluric exploration to rock samples. Geophys. Prospect. 64 (2), 469–488.

Alvarez, P., Marcy, F., Vrijlandt, M., Skinnemoen, Ø., MacGregor, L., Nichols, K., Keirstead, R., Bolivar, F., Bouchrara, S., Smith, M., 2018. Multi-physics characterisation of reservoir prospects in the Hoop area of the Barents Sea. Interpretation 6, 1–51.

Amantov, A., Fjeldskaar, W., 2018. Meso-Cenozoic exhumation and relevant isostatic process: the Barents and Kara shelves. J. Geodyn. 118, 118–139.

Anell, I., Braathen, A., Olaussen, S., 2014. The triassic-early jurassic of the northern Barents shelf: a regional understanding of the longyearbyen CO_2 reservoir. Norw. J. Geol. 94, 83–98.

Aquino-López, A., Mousatov, A., Markov, M., 2011. Model of sand formations for joint simulation of elastic moduli and electrical conductivity. J. Geophys. Eng. 8, 568–578.

Archie, G.E., 1942. The electrical resistivity log as an aid in determining some reservoir characteristics. Petroleum Technology 1422, 54–62.

Baig, I., Faleide, J.I., Jahren, J., Mondol, N.H., 2016. Cenozoic exhumation on the southwestern Barents Shelf: estimates and uncertainties constrained from compaction and thermal maturity analyses. Mar. Petrol. Geol. 73, 105–130.

Baltar, D., Barker, N.D., 2015. Prospectivity evaluation with 3D CSEM. First Break 33, 55–62.

Baltar, D., Roth, F., 2013. Reserves estimation methods for prospect evaluation with 3D CSEM data. First Break 31, 103–111.

Barker, N., Baltar, D., 2016. CSEM anomaly identification. First Break 34, 47–50.

Birchall, T., Senger, K., Hornum, M., Olaussen, S., Braathen, A., 2020. Underpressure in the northern Barents shelf: Causes and implications for hydrocarbon exploration. AAPG Bull. https://doi.org/10.1306/02272019146. http://archives.datapages.com/data/bulletns/aop/2020-07-20/aapgbltn19146aop.html.

Blixt, E.M., Storvoll, V., Olstad, R., 2017. A statistical sensitivity method for CSEM—implications for petroleum exploration in the Barents Sea. First Break 35, 37–44.

Buland, A., Løseth, L.O., Becht, A., Roudot, M., Røsten, T., 2011. The value of CSEM data in exploration. First Break 29, 69–76.

Cameron, D., Read, D., Jong, E.D., Oosterveld, M., 1981. Mapping salinity using resistivity and electromagnetic inductive techniques. Can. J. Soil Sci. 61, 67–78.

Carcione, J., Ursin, B., Nordskag, J., 2007. Cross-property relations between electrical conductivity and the seismic velocity of rocks. Geophysics 72, E193–E204.

Carstens, H., 2018. An Important Discovery, p. Geo365. https://geo365.no/olje-og-gass/an-important-discovery/.

Cartwright, J., Huuse, M., 2005. 3D seismic technology: the geological 'Hubble'. Basin Res. 17, 1–20.
Cavanagh, A.J., Di Primio, R., Scheck-Wenderoth, M., Horsfield, B., 2006. Severity and timing of cenozoic exhumation in the southwestern Barents Sea. J. Geol. Soc. 163, 761–774.
Clavaud, J.-B., 2008. Intrinsic electrical anisotropy of shale: the effect of compaction. Petrophysics 49, 243–260.
Constable, S., 2010. Ten years of marine CSEM for hydrocarbon exploration. Geophysics 75, 75A67–75A81.
Dimakis, P., Braathen, B.I., Faleide, J.I., Elverhøi, A., Gudlaugsson, S.T., 1998. Cenozoic erosion and the preglacial uplift of the Svalbard–Barents Sea region. Tectonophysics 300, 311–327.
Duran, E.R., di Primio, R., Anka, Z., Stoddart, D., Horsfield, B., 2013. 3D-basin modelling of the Hammerfest Basin (southwestern Barents Sea): a quantitative assessment of petroleum generation, migration and leakage. Mar. Petrol. Geol. 45, 281–303.
Eidesmo, T., Ellingsrud, S., MacGregor, L.M., Constable, S., Sinha, M.C., Johansen, S., Kong, F.N., Westerdahl, H., 2002. Sea Bed Logging (SBL), a new method for remote and direct identification of hydrocarbon filled layers in deepwater areas. First Break 20, 144–152.
Ellingsrud, S., Eidesmo, T., Johansen, S., Sinha, M., MacGregor, L., Constable, S., 2002. Remote sensing of hydrocarbon layers by seabed logging (SBL): results from a cruise offshore Angola. Lead. Edge 21, 972–982.
Ellis, M., MacGregor, L., Newton, P., Keirstead, R., Bouchrara, S., Zhou, Y., Tseng, H., 2017. Investigating electrical anisotropy drivers across the Barents Sea. In: 79th EAGE Conference and Exhibition 2017, 12-15 June, Paris, France.
Ellis, M., Sinha, M., Parr, R., 2010a. Role of fine-scale layering and grain alignment in the electrical anisotropy of marine sediments. First Break 28, 49–57.
Ellis, M.H., Sinha, M.C., Minshull, T.A., Sothcott, J., Best, A.I., 2010b. An anisotropic model for the electrical resistivity of two-phase geologic materials. Geophysics 75, E161–E170.
Evans, R.L., 2007. Using CSEM techniques to map the shallow section of seafloor: from the coastline to the edges of the continental slopeShallow-section EM mapping. Geophysics 72, WA105–WA116.
Faleide, J.I., Solheim, A., Fiedler, A., Hjelstuen, B.O., Andersen, E.S., Vanneste, K., 1996. Late Cenozoic evolution of the western Barents Sea-Svalbard continental margin. Global Planet. Change 12, 53–74.
Faleide, J.I., Tsikalas, F., Breivik, A.J., Mjelde, R., Ritzmann, O., Engen, Ø., Wilson, J., Eldholm, O., 2008. Structure and evolution of the continental margin off Norway and the Barents Sea. Episodes 31, 82–91.
Faleide, J.I., Vågnes, E., Gudlaugsson, S.T., 1993. Late Mesozoic-Cenozoic evolution of the south-western Barents Sea in a regional rift-shear tectonic setting. Mar. Petrol. Geol. 10, 186–214.
Fanavoll, S., Gabrielsen, P., Ellingsrud, S., 2014. CSEM as a tool for better exploration decisions: case studies from the Barents Sea. Norwegian Continental Shelf. Interpretation 2, SH55–SH66.
Gabrielsen, P.T., Abrahamson, P., Panzner, M., Fanavoll, S., Ellingsrud, S., 2013. Exploring frontier areas using 2D seismic and 3D CSEM data, as exemplified by multi-client data over the Skrugard and Havis discoveries in the Barents Sea. First Break 31, 63–71.
Gelius, L.-J., Wang, Z., 2008. Modelling production caused changes in conductivity for a siliciclastic reservoir: a differential effective medium approach. Geophys. Prospect. 56, 677–691.
Glørstad-Clark, E., Faleide, J.I., Lundschien, B.A., Nystuen, J.P., 2010. Triassic seismic sequence stratigraphy and paleogeography of the western Barents Sea area. Mar. Petrol. Geol. 27, 1448–1475.
Goswami, B.K., Weitemeyer, K.A., Bünz, S., Minshull, T.A., Westbrook, G.K., Ker, S., Sinha, M.C., 2017. Variations in pockmark composition at the Vestnesa Ridge: insights from marine controlled source electromagnetic and seismic data. G-cubed 18, 1111–1125.
Granli, J.R., Veire, H.H., Gabrielsen, P., Morten, J.P., 2017. Maturing Broadband 3D CSEM for Improved Reservoir Property Prediction in the Realgrunnen Group at Wisting, Barents Sea, SEG Technical Program Expanded Abstracts 2017. Society of Exploration Geophysicists, pp. 2205–2209.
Grogan, P., Østvedt-Ghazi, A.M., Larssen, G.B., Fotland, B., Nyberg, K., Dahlgren, S., Eidvin, T., 1999. Structural elements and petroleum geology of the Norwegian sector of the northern Barents Sea. Geological Society, London, Petroleum Geology Conference series 5, 247–259.
Grundvåg, S.-A., Marin, D., Kairanov, B., Śliwińska, K., Nøhr-Hansen, H., Escalona, A., Olaussen, S., 2017. The lower cretaceous succession of the northwestern Barents shelf: onshore and offshore correlations. Mar. Petrol. Geol. 86, 834–857.
Han, D.-H., Batzle, M., 2002. Fizz water and low gas-saturated reservoirs. Lead. Edge 21, 395–398.
Han, T., Best, A.I., Sothcott, J., North, L.J., MacGregor, L.M., 2015. Relationships among low frequency (2 Hz) electrical resistivity, porosity, clay content and permeability in reservoir sandstones. J. Appl. Geophys. 112, 279–289.
Henriksen, E., Bjørnseth, H.M., Hals, T.K., Heide, T., Kiryukhina, T., Kløvjan, O.S., Larssen, G.B., Ryseth, A.E., Rønning, K., Sollid, K., Stoupakova, A., 2011a. Chapter 17 Uplift and erosion of the greater Barents Sea: impact on prospectivity and petroleum systems. In: Spencer, A.M., Embry, A.F., Gautier, D.L., Stoupakova, A.V., Sørensen, K. (Eds.), Arctic Petroleum Geology. The Geological Society, London, pp. 271–281.
Henriksen, E., Ryseth, A.E., Larssen, G.B., Heide, T., Rønning, K., Sollid, K., Stoupakova, A.V., 2011b. Chapter 10 Tectonostratigraphy of the greater Barents Sea: implications for petroleum systems. In: Spencer, A.M., Embry, A.F., Gautier, D.L., Stoupakova, A.V., Sørensen, K. (Eds.), Arctic Petroleum Geology. The Geological Society, London, pp. 163–195.
Hesthammer, J., Stefatos, A., Boulaenko, M., Fanavoll, S., Danielsen, J., 2010. CSEM performance in light of well results. Lead. Edge 29, 34–41.
Høy, T., Lundschien, B.A., 2011. Chapter 15 triassic deltaic sequences in the northern Barents Sea. In: Spencer, A.M., Embry, A.F., Gautier, D.L., Stoupakova, A.V., Sørensen, K. (Eds.), Arctic Petroleum Geology. Geological Society, Memoir #35, London, pp. 249–260.
Jakobsson, K., 2018. A history of exploration offshore Norway: the Barents Sea. Geological Society, London, Special Publications 465. SP465. 418.
Johansen, S., Gabrielsen, P., 2015. Interpretation of marine CSEM and marine MT data for hydrocarbon prospecting. In: Bjørlykke, K. (Ed.), Petroleum Geoscience. Springer Berlin Heidelberg, pp. 515–544.
Johansen, S.E., Panzner, M., Mittet, R., Amundsen, H.E., Lim, A., Vik, E., Landrø, M., Arntsen, B., 2019. Deep electrical imaging of the ultraslow-spreading Mohns Ridge. Nature 567, 379.
Johnson, H.M., 1962. A history of well logging. Geophysics 27, 507–527.
Kethireddy, N., Chen, H., Heidari, Z., 2014. Quantifying the effect of kerogen on resistivity measurements in organic-rich mudrocks. Petrophysics 55, 136–146.
Klausen, T.G., Müller, R., Poyatos-Moré, M., Olaussen, S., Stueland, E., 2019a. Tectonic, provenance and sedimentological controls on reservoir characteristics in the upper triassic–middle jurassic realgrunnen Subgroup, SW Barents Sea. Geological Society, London, Special Publications 495. SP495-2018-2165.
Klausen, T.G., Müller, R., Slama, J., Helland-Hansen, W., 2017. Evidence for late triassic provenance areas and early jurassic sediment supply turnover in the Barents Sea basin of northern pangea. Lithosphere 9, 14–28.
Klausen, T.G., Nyberg, B., Helland-Hansen, W., 2019c. The largest delta plain in Earth's history. Geology 47, 470–474.
Koevoets, M.J., Hammer, Ø., Olaussen, S., Senger, K., Smelror, M., 2019. Integrating subsurface and outcrop data of the Middle jurassic to lower cretaceous agardfjellet Formation in central spitsbergen. Norw. J. Geol. 98, 1–34.
Ktenas, D., Henriksen, E., Meisingset, I., Nielsen, J.K., Andreassen, K., 2017. Quantification of the magnitude of net erosion in the southwest Barents Sea using sonic velocities and compaction trends in shales and sandstones. Mar. Petrol. Geol. 88, 826–844.
Lasabuda, A., Geissler, W.H., Laberg, J.S., Knutsen, S.M., Rydningen, T.A., Berglar, K., 2018. Late Cenozoic erosion estimates for the northern Barents Sea: quantifying glacial sediment input to the Arctic Ocean. G-cubed 19, 4876–4903.
Lerch, B., Karlsen, D.A., Thieβen, O., Abay, T.B., van Soelen, E.E., Kürschner, W.M., Planke, S., Backer-Owe, K., 2018. Investigations on the use of triaromatic dimethylcholesteroids as age-specific biomarkers in bitumens and oils from Arctic Norway. Org. Geochem. 122, 1–16.
Lundschien, B.A., Høy, T., Mørk, A., 2014. Triassic hydrocarbon potential in the Northern Barents Sea; integrating Svalbard and stratigraphic core data. Norwegian Petroleum Directorate Bulletin 11, 3–20.
Løseth, L.O., Wiik, T., Olsen, P.A., Hansen, J.O., 2014. Detecting Skrugard by CSEM — prewell prediction and postwell evaluation. Interpretation 2 (3), SH67–SH78.
MacGregor, L., 2012. Integrating seismic, CSEM, and well-log data for reservoir characterization. Lead. Edge 268–277.
MacGregor, L., Bouchrara, S., Tomlinson, J., Strecker, U., Fan, J., Ran, X., Yu, G., 2012. Integrated analysis of CSEM, seismic and well log data for prospect appraisal: a case study from West Africa. First Break 30, 43–48.
MacGregor, L., Tomlinson, J., 2014. Marine controlled-source electromagnetic methods in the hydrocarbon industry: a tutorial on method and practice. Interpretation 2, SH13–SH32.
Matapour, Z., Karlsen, D., Lerch, B., Backer-Owe, K., 2019. Petroleum occurrences in the carbonate lithologies of the Gohta and Alta discoveries in the Barents Sea, arctic Norway. Petrol. Geosci. 25, 50–70.
McCarthy, K., Rojas, K., Niemann, M., Palmowski, D., Peters, K., Stankiewicz, A., 2011. Basin petroleum geochemistry for source rock evaluation. Oilfield Rev. 23, 32–43.
Midtkandal, I., Faleide, J.I., Faleide, T.S., Serck, C.S., Planke, S., Corseri, R., Dimitriou, M., Nystuen, J.P., 2020. Lower Cretaceous Barents Sea strata: epicontinental basin configuration, timing, correlation and depositional dynamics. Geol. Mag. 157 (3), 458–476.
Moran, J., Gianzero, S., 1979. Effects of formation anisotropy on resistivity-logging measurements. Geophysics 44, 1266–1286.
Mulrooney, M.J., Leutscher, J., Braathen, A., 2017. A 3D structural analysis of the Goliat field, Barents Sea, Norway. Mar. Petrol. Geol. 86, 192–212.
Müller, R., Klausen, T., Faleide, J., Olaussen, S., Eide, C., Suslova, A., 2019. Linking regional unconformities in the Barents Sea to compression-induced forebulge uplift at the Triassic-Jurassic transition. Tectonophysics 765, 35–51.
Mørk, M.B.E., 2013. Diagenesis and quartz cement distribution of low-permeability Upper Triassic –Middle Jurassic reservoir sandstones, Longyearbyen CO_2 lab well site in Svalbard, Norway. AAPG (Am. Assoc. Pet. Geol.) Bull. 97, 577–596.
Newman, G., Commer, M., Carazzone, J., 2010. Imaging CSEM data in the presence of electrical anisotropy. Geophysics 75, F51–F61.
North, L., Best, A.I., Sothcott, J., MacGregor, L., 2013. Laboratory determination of the full electrical resistivity tensor of heterogeneous carbonate rocks at elevated pressures. Geophys. Prospect. 61, 458–470.
North, L.J., Best, A.I., 2014. Anomalous electrical resistivity anisotropy in clean reservoir sandstones. Geophys. Prospect. 62, 1315–1326.
NPD, 2015. Resource accounts for the Norwegian continental shelf as of 31 December 2015. http://www.npd.no/en/Topics/Resource-accounts-and–analysis/Temaartikler/Resource-accounts/2015/.
NPD, 2019. FactPages accessed 01.08.2019.
Nøttvedt, A., Livbjerg, F., Midbøe, P.S., Rasmussen, E., 1993. Hydrocarbon potential of the central spitsbergen basin. In: Vorren, T.O., Bergsager, E., Dahl-Stamnes, Ø.A.,

Holter, E., Johansen, B., Lie, E., Lund, T.B. (Eds.), Arctic Geology and Petroleum Potential. Elsevier, Amsterdam, pp. 333–361.
Ohm, S.E., Karlsen, D.A., Austin, T.J.F., 2008. Geochemically driven exploration models in uplifted areas: examples from the Norwegian Barents Sea. AAPG (Am. Assoc. Pet. Geol.) Bull. 92, 1191–1223.
Olaussen, S., Larssen, G., Helland-Hansen, W., Johannessen, E., Nøttvedt, A., Riis, F., Rismyhr, B., Smelror, M., Worsley, D., 2018. Mesozoic strata of kong karls land, svalbard, Norway; a link to the northern Barents Sea basins and platforms. Norw. J. Geol. 98, 1–69. https://doi.org/10.17850/njg98-4-06.
Olsen, P.A., 2011. Coarse-scale resistivity for saturation estimation in heterogeneous reservoirs based on Archie's formula. Geophysics 76, E35–E43.
OMV, 2019. Increased Wisting Volumes.
Passey, Q., Creaney, S., Kulla, J., Moretti, F., Stroud, J., 1990. A practical model for organic richness from porosity and resistivity logs. AAPG Bull. 74, 1777–1794.
Pridmore, D., Shuey, R., 1976. The electrical resistivity of galena, pyrite, and chalcopyrite. Am. Mineral. 61, 248–259.
Revil, A., Cathles, L.M., Losh, S., Nunn, J.A., 1998. Electrical conductivity in shaly sands with geophysical applications. J. Geophys. Res.: Solid Earth 103, 23925–23936.
Rossi, V.M., Olaussen, S., Staine, I.N., Gennaro, M., 2020. Development of the Middle triassic kobbe Formation shelf-margin prism and transgressive-regressive cycles on the shelf (Hammerfest Basin, SW Barents Sea). Mar. Petrol. Geol. 111, 868–885.
Rudnicki, M.D., 2016. Variation of organic matter density with thermal maturity. AAPG (Am. Assoc. Pet. Geol.) Bull. 100, 17–22.
Ryseth, A., 2014. Sedimentation at the jurassic–triassic boundary, south-west Barents Sea. In: From Depositional Systems to Sedimentary Successions on the Norwegian Continental Margin. John Wiley & Sons, Ltd, pp. 187–214.
Rønnevik, H.C., 2015. Exploration strategy. In: Bjørlykke, K. (Ed.), Petroleum Geoscience. Springer, pp. 639–651.
Salem, H.S., Chilingarian, G.V., 1999. The cementation factor of Archie's equation for shaly sandstone reservoirs. J. Petrol. Sci. Eng. 23, 83–93.
Schneider, R.V., Bouchrara*, S., MacGregor, L., Alvarez, A., Ellis, M., Ackermann, R., Newton, P., Keirstead, R., Rusic, A., Zhou, Y., 2015. CSEM based anisotropy trends in the Barents Sea. In: SEG Technical Program Expanded Abstracts 2015. Society of Exploration Geophysicists, pp. 879–883.
Schwalenberg, K., Rippe, D., Koch, S., Scholl, C., 2017. Marine-controlled source electromagnetic study of methane seeps and gas hydrates at Opouawe Bank, Hikurangi Margin, New Zealand. J. Geophys. Res.: Solid Earth 122, 3334–3350.
Sen, P., Goode, P., 1992. Influence of temperature on electrical conductivity on shaly sands. Geophysics 57, 89–96.
Senger, K., Birchall, T., Ohm, S., Ogata, K., Olaussen, S., 2017a. Review of geological controls on resistivity in uplifted basins: insights from the Norwegian Barents shelf. In: AAPG International Conference & Exhibition, London, UK, 15-18 October 2017, p. 10.
Senger, K., Brugmans, P., Grundvåg, S.-A., Jochmann, M., Nøttvedt, A., Olaussen, S., Skotte, A., Smyrak-Sikora, A., 2019. Petroleum, coal and research drilling onshore Svalbard: a historical perspective. Norw. J. Geol. 99 (3), 1–30.
Senger, K., Millett, J., Planke, S., Ogata, K., Eide, C., Festøy, M., Galland, O., Jerram, D., 2017b. Effects of igneous intrusions on the petroleum system: a review. First Break 35, 10.
Senger, K., Svendsen, R., Gabrielsen, P., Fanavoll, S., Pedersen, C.B., Kjølhamar, B., 2015. Regional Resistivity Trends in the Northern Barents Sea: Insights from CSEM Data. Norsk Geologisk Vinterkonferansen 12-14.1.2015, Stavanger, Norway.
Senger, K., Tveranger, J., Ogata, K., Braathen, A., Planke, S., 2014. Late mesozoic magmatism in svalbard: a review. Earth Sci. Rev. 139, 123–144.
Serck, C.S., Faleide, J.I., Braathen, A., Kjølhamar, B., Escalona, A., 2017. Jurassic to early cretaceous basin configuration (s) in the fingerdjupet subbasin, SW Barents Sea. Mar. Petrol. Geol. 86, 874–891.
Shephard, G.E., Müller, R.D., Seton, M., 2013. The tectonic evolution of the Arctic since Pangea breakup: integrating constraints from surface geology and geophysics with mantle structure. Earth Sci. Rev. 124, 148–183.
Spacapan, J.B., D'Odorico, A., Palma, O., Galland, O., Senger, K., Ruiz, R., Manceda, R., Leanza, H.A., 2019. Low resistivity zones at contacts of igneous intrusions emplaced in organic-rich formations and their implications on fluid flow and petroleum systems: a case study in the northern Neuquén Basin, Argentina. Basin Res. 32, 3–24.
Steel, R.J., Worsley, D., 1984. Svalbard's post-Caledonian strata - an atlas of sedimentational patterns and paleogeographic evolution. In: Spencer, A.M. (Ed.), Petroleum Geology of the North European Margin. Graham & Trotman, London, pp. 109–135.
Stefatos, A., Vereshagin, A., Hesthammer, J., Kalstø, T., Sperrevik, S., Robson, A., 2014. CSEM-driven exploration over the nordland ridge. Interpretation 2, SH79–SH95.
Tharimela, R., Augustin, A., Ketzer, M., Cupertino, J., Miller, D., Viana, A., Senger, K., 2019. 3D controlled-source electromagnetic imaging of gas hydrates: insights from the Pelotas Basin offshore Brazil. Interpretation 7, SH111–SH131.
Vereshagin, A., Wedberg, T., Stefatos, A., 2019. Predicting vertical resistivity by machine learning. In: 81st EAGE Conference and Exhibition 2019. European Association of Geoscientists & Engineers, pp. 1–5.
Wedberg, T., Stefatos, A., Vereshagin, A., 2017. Up scaling of triaxial resistivity data measured on the Norwegian Continental Shelf and observations relevant for CSEM imaging. In: AAPG/SEG Conference and Exhibition. Search and Discovery Article #90310, London, England.
Weitemeyer, K.A., Constable, S., Tréhu, A.M., 2011. A marine electromagnetic survey to detect gas hydrate at Hydrate Ridge, Oregon. Geophys. J. Int. 187, 45–62.
Wennberg, O.P., Malm, O., Needham, T., Edwards, E., Ottesen, S., Karlsen, F., Rennan, L., Knipe, R., 2008. On the occurrence and formation of open fractures in the Jurassic reservoir sandstones of the Snøhvit Field, SW Barents Sea. Petrol. Geosci. 14, 139–150.
Werthmüller, D., Ziolkowski, A., Wright, D., 2013. Background resistivity model from seismic velocities. Geophysics 78, E213–E223.
Worsley, D., 2008. The post-Caledonian development of Svalbard and the western Barents Sea. Polar Res. 27, 298–317.
Worthington, P.F., 1982. The influence of shale effects upon the electrical resistivity of reservoir rocks. Geophys. Prospect. 30, 673–687.
Worthington, P.F., 1993. The uses and abuses of the Archie equations, 1: the formation factor-porosity relationship. J. Appl. Geophys. 30, 215–228.
Worthington, P.F., 2000. Recognition and evaluation of low-resistivity pay. Petrol. Geosci. 6, 77–92.
Yang, A., Firdaus, G., Heidari, Z., 2016. Electrical resistivity and chemical properties of kerogen isolated from organic-rich mudrocks. Geophysics 81, D643–D655.
Zhao, H., Givens, N.B., Curtis, B., 2007. Thermal maturity of the Barnett Shale determined from well-log analysis. AAPG Bull. 91, 535–549.
Ziarani, A.S., Aguilera, R., 2012. Pore-throat radius and tortuosity estimation from formation resistivity data for tight-gas sandstone reservoirs. J. Appl. Geophys. 83, 65–73.
Zweidler, D., Baltar, D., Barker, N., 2015. Impact of CSEM on Return of Exploration Investment. Hart's E&P.